AGU ADVANCING EARTH AND SPACE SCIENCE

Geochemistry, Geophysics, Geosystems®

RESEARCH ARTICLE
10.1029/2021GC009924

Key Points:
- Updated modeling and observations of lowermost mantle seismic anisotropy beneath Siberia
- We combine different data types to constrain seismic anisotropy mechanisms and plausible flow directions beneath Siberia
- Post-perovskite is the likely mechanism with a slightly dipping shear plane and shear direction toward the northeast/southwest

Supporting Information:
Supporting Information may be found in the online version of this article.

Correspondence to:
N. Creasy,
nmcreasy@mines.edu

Citation:
Creasy, N., Pisconti, A., Long, M. D., & Thomas, C. (2021). Modeling of seismic anisotropy observations reveals plausible lowermost mantle flow directions beneath Siberia. *Geochemistry, Geophysics, Geosystems*, *22*, e2021GC009924. https://doi.org/10.1029/2021GC009924

Received 25 MAY 2021
Accepted 25 SEP 2021

Modeling of Seismic Anisotropy Observations Reveals Plausible Lowermost Mantle Flow Directions Beneath Siberia

Neala Creasy[1], Angelo Pisconti[2], Maureen D. Long[3], and Christine Thomas[2]

[1]Department of Geophysics, Colorado School of Mines, Golden, CO, USA, [2]University of Muenster, Muenster, Germany, [3]Department of Earth and Planetary Sciences, Yale University, New Haven, CT, USA

Abstract Observations of seismic anisotropy just above the core-mantle boundary are a powerful way to understand the dynamics of the lowermost mantle. Here we present models of seismic anisotropy in the lowermost mantle beneath Siberia based on new and previously published body wave observations. We compile a set of measurements based on a variety of data types, including the differential splitting of SK(K)S-PKS and S-ScS phases and polarities of PdP and SdS reflections off the D″ discontinuity. We carry out ray theoretical forward modeling of these data sets in combination, using a novel approach that allows for tighter constraints on the geometry of seismic anisotropy than would be possible using a single data type. Observations for each seismic phase alone only provide limited information; by combining different data types into one modeling approach, we can constrain D″ seismic anisotropy more tightly. We test a range of plausible mechanisms for seismic anisotropy, including a variety of candidate minerals (bridgmanite, post-perovskite, and ferropericlase), dominant slip systems, and orientations, and consider both single-crystal elasticity and elastic tensors based on polycrystalline texture modeling. In general, we find that post-perovskite (with either a [100](010) or [100](001) dominant slip system) or bridgmanite models provide the best fit to the observations. The best-fitting models suggest a dominant shear direction to the southwest or northeast direction at the base of the mantle. This is consistent with flow directed toward the Perm anomaly, potentially driven by slab remnants impinging on the core-mantle boundary.

1. Introduction

Observations of seismic anisotropy are a powerful tool for mapping deformation within the Earth (e.g., Long & Becker, 2010), and are often used to study deformation and flow in the upper mantle (e.g., Skemer & Hansen, 2016). The lowermost mantle, also known as the D″ layer, also clearly exhibits seismic anisotropy (e.g., Garnero & Lay, 1997; Kendall & Silver, 1996, and references within Nowacki et al., 2011; Romanowicz & Wenk, 2017), and seismic anisotropy observations can be used to map deformation at the base of the mantle. However, this requires thorough knowledge of the mechanism for D″ seismic anisotropy and the relationship between deformation and strain, which can be established by experiments and theoretical modeling. There are several proposed mechanisms for D″ seismic anisotropy, including the shape preferred orientation (SPO) of melt inclusions (or other elastically distinct material) and the crystallographic preferred orientation (CPO) of bridgmanite (bm), ferropericlase (fp), post-perovskite (ppv), or some mixture of these minerals (e.g., Nowacki et al., 2011).

A major obstacle in the interpretation of D″ seismic anisotropy measurements is our imprecise knowledge of the mechanism responsible, along with the non-uniqueness of data sets that are based on a limited number of measurements in a given region. A recent synthetic modeling study (Creasy et al., 2019) demonstrated that tighter constraints on seismic anisotropy at the base of the mantle can be obtained by combining different types of observations of body wave anisotropy than by a single type of data alone. Specifically, Creasy et al. (2019) examined reflection polarity measurements (P or S waves that reflect off the D″ discontinuity–PdP and SdS) and shear wave splitting (seismic wave birefringence). In this study, we apply the insights gained from the synthetic modeling of Creasy et al. (2019) and combine observations of shear wave splitting (for both ScS and PKS phases) due to D″ seismic anisotropy with observations of PdP/SdS polarities (and their variation with direction) to obtain tight constraints on geometry in a single target region. We apply a novel modeling approach that is based on previous work (Creasy et al., 2017; Ford et al., 2015) and has been

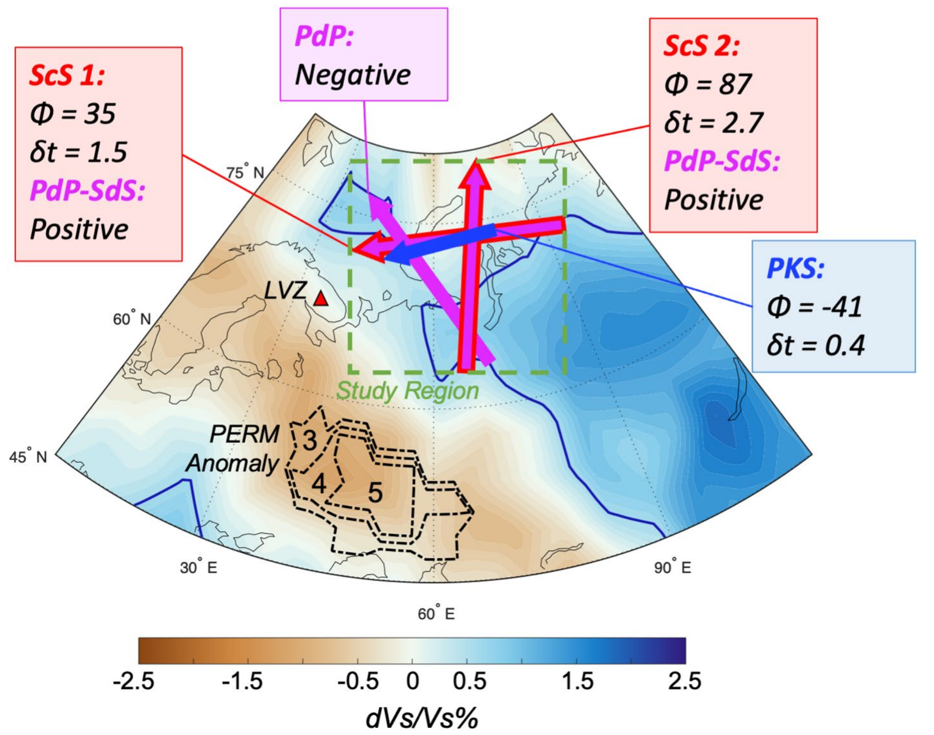

Figure 1. Geographic setting and summary of observations used in this study. Arrows represent the approximate raypaths for each phase (averaged over multiple measurements); we also show the reflection polarities and the average shear wave splitting parameters in a ray-centered reference frame (red = ScS splitting, magenta = reflection polarities, blue = PKS splitting). Color scale shows the S wave velocity perturbation (dVs/Vs%) in the GyPSuM tomography model (Simmons et al., 2009) at 2,800 km depth. Faster than average (>0.5%) regions are highlighted by the dark blue line. Black dotted lines represent different representations of the edges of the Perm Anomaly, based on the cluster model cutoffs of Lekic et al. (2012). Labels indicate the number of tomography models (out of a possible 5) that agree that the mantle is unusually slow for that region.

expanded to accommodate a range of data types, combining reflection polarity modeling and shear wave splitting in the same modeling framework. This approach helps to ameliorate the non-uniqueness problem that is a common challenge in the study of lowermost mantle seismic anisotropy (Pisconti et al., 2019).

Our study targets the lowermost mantle beneath Siberia (specifically beneath the Kara Sea; Figure 1). Because of its geographic location, this region can be probed for D″ seismic anisotropy using various favorable configurations of earthquake sources and receivers, including those that are part of dense seismic arrays. Previous studies of the lowermost mantle beneath Siberia have found robust evidence for seismic anisotropy from differential S-ScS splitting (Thomas & Kendall, 2002; Wookey & Kendall, 2008), differential SKS-SKKS splitting (Grund & Ritter, 2019; Long & Lynner, 2015), Scd (lower mantle triplication) travel times (Tao et al., 2020), and reflection polarity measurements (Thomas et al., 2011). Specifically, Thomas et al. (2011) measured the polarity of PdP and SdS reflections over multiple paths and interpreted changes in polarity with propagation direction as reflecting seismic anisotropy within the D″ layer. The differential S-ScS splitting study of Wookey and Kendall (2008) accounted for upper mantle contributions to splitting of ScS waveforms (on both the source and receiver side) and isolated D″-associated shear wave splitting for two unique propagation paths (at different azimuths) beneath Siberia. Long and Lynner (2015) and Grund and Ritter (2019) identified discrepant SKS-SKKS splitting for phases that sample the lowermost mantle beneath Siberia, suggesting a contribution from seismic anisotropy in the lowermost mantle to the shear wave splitting of one or both phases. Long and Lynner (2015) suggested a particularly prominent signal due to seismic anisotropy near the Perm Anomaly (Figure 1). The Perm anomaly lies within our study region, just to the southwest of the region sampled by the Wookey and Kendall (2008) and Thomas et al. (2011) seismic observations. The Perm anomaly (Lekic et al., 2012; Cottaar & Lekic, 2016, Figure 1) is a region of reduced seismic shear velocities just above the core-mantle boundary (CMB) that has similar seismic properties to (although smaller dimensions than) the African and Pacific Large Low Shear Velocity Provinces (LLSVPs). Our study targets a particular region of the lowermost mantle beneath the Kara Sea and uses observations from the Thomas et al. (2011) and Wookey and Kendall (2008) studies, in combination with new observations of the shear wave splitting of core phases (particularly PKS) that sample the same region as this previous work.

While Wookey and Kendall (2008) and Thomas et al. (2011) sampled a similar portion of the lowermost mantle, they came to slightly different conclusions about possible deformation geometries based on different types of observations. Wookey and Kendall (2008) found that while their data could not identify a single unique mechanism or seismic anisotropic geometry, deformed post-perovskite with a dominant [100](010) slip system, or aligned melt inclusions, could best explain their observations. In either case, the shear direction most consistent with the data was found to be nearly north south, with a dipping shear plane preferred by the observations. Thomas et al. (2011) investigated a more limited set of models than Wookey and Kendall (2008), focusing on aligned bridgmanite or post-perovskite models and choosing shear planes oriented in a (geodynamically plausible) east-west shear direction. They identified a preference for post-perovskite with the same dominant slip system as that favored by Wookey and Kendall (2008)—[100](010)—but with an east-west shear direction. Nowacki (2013) revisited the Siberia shear wave splitting datasets of Wookey and Kendall (2008) with new models of seismic anisotropy based on global flow models (Walker et al., 2011). This study used predictions from a global geodynamic flow model to compare S-ScS splitting to three different slip planes of post-perovskite. The global mantle flow model (e.g., Simmons et al., 2009) predicted flow at the core-mantle boundary toward the west. Nowacki (2013) found a preference for post-perovskite with slip on the (010) plane beneath our study region.

There is a long and complicated history of the subduction of material into the deep mantle beneath Siberia; this history is constrained by studies of the seismic structure and geodynamical modeling. Global tomographic models of lowermost mantle generally agree that the region is seismically fast in Vp and Vs (Cottaar & Lekic, 2016), discussed further below. A number of more focused seismic studies have been aimed at constraining the (an)isotropic structure of the D″ layer within this region as well (Nataf & Houard, 1993; Scherbaum et al., 1997; Tao et al., 2020; Weber, 1993). For example, Tao et al. (2020) used observations of lowermost mantle triplication data, and previous seismic anisotropy studies, to suggest that just to the south of our study region, flow at the base of the mantle is likely driven by a remnant of the Mongol-Kazakh/Okhotsk subducted slab and directed to the west-southwest, toward the Perm anomaly. The Mongol-Okhotsk slab is currently located beneath northern Siberia, where the Mongol-Okhotsk ocean began to subduct some time before 251 Ma (Tomurtogoo et al., 2005), with subduction continuing up to ∼145 Ma (Van der Voo et al., 1999). Time-dependent global geodynamical models of mantle flow (Fritzell et al., 2016; Shephard et al., 2014) suggest that the Mongol-Okhotsk slab has been migrating toward the west as it sinks, and that the slab remnants are currently located at ∼2,850 km depth (just ∼41 km above the CMB) to the southeast of our study region beneath the Kara Sea. Based on global tomography models, van der Meer et al. (2018) suggested the presence of additional possible slab remnants in the deep mantle just to the north of our study region, specifically the Komsomolets slab (2,200 km deep). These structures in the lowermost mantle (including slab remnants and the Perm anomaly) all likely influence deep mantle flow.

The goal of this study is to better constrain the present-day pattern of flow at the base of the mantle beneath Siberia and interpret that flow pattern in the context of the complex subduction history. To do this, we carry out detailed forward modeling of body wave observations of lowermost mantle seismic anisotropy in our study region. We augment previously published datasets (Thomas & Weber, 1997; Thomas et al., 2011; Wookey & Kendall, 2008), including observations of ScS splitting and of SdS and PdP reflection polarities, with new observations of the shear wave splitting of core phases due to lowermost mantle seismic anisotropy. Using the framework suggested by Creasy et al. (2019), we jointly model our set of (previously published and new) observations of different types to identify seismic anisotropy models that simultaneously satisfy the full suite of available data. We find that the combination of different types of data allow us to place tighter constraints on the range of allowable seismic anisotropy scenarios than would be possible with a single type of observations and enables us to connect plausible seismic anisotropy scenarios to possible mantle flow geometries.

10.1029/2021GC009924

2. New Seismic Anisotropy Measurements Beneath Siberia: Data and Methods

In order to augment the previous measurements of Wookey and Kendall (2008), Thomas and Weber (1997), and Thomas et al. (2011), we aimed to identify any possible contributions to the splitting of shear core-refracted phases (potentially including SKS, SKKS, PKS and SKiKS) from lowermost mantle seismic anisotropy in our study region. The widespread presence of seismic anisotropy in the upper mantle presents challenges for isolating the contribution from seismic anisotropy at the base of the mantle. A common approach to circumvent this challenge is to measure the differential shear wave splitting of pairs of phases with similar paths in the upper mantle but different paths in the lower mantle. To explicitly correct for the contribution from upper mantle seismic anisotropy beneath the station for the lowermost mantle seismic anisotropy measurements presented in this paper, we use measurements of SK(K)S splitting over a range of backazimuths. This approach assumes that there is no significant contribution to shear wave splitting from the bulk of the lower mantle (Meade et al., 1995). This type of upper mantle correction has been applied to measure the differential splitting of S-ScS phases (Pisconti et al., 2019; Rao & Kumar, 2014; Wolf et al., 2015; Wookey et al., 2005). In such studies, SKS phases constrain upper mantle contributions beneath the receiver, while direct S constrains splitting near the source; any differential splitting exhibited by ScS after the proper corrections can then be attributed to the lowermost mantle. Differential measurements of SKS-SKKS splitting can also reflect a contribution from the lowermost mantle (e.g., Grund & Ritter, 2019; He & Long, 2011; Long, 2009; Long & Lynner, 2015; Niu & Perez, 2004; Reiss et al., 2019); in some cases, explicit corrections for the upper mantle contribution are applied (e.g., Ford et al., 2015; Long & Lynner, 2015; Lynner & Long, 2014).

Previous studies of deep mantle seismic anisotropy have shown the importance of selecting stations that overlie either simple (a single, laterally homogeneous layer) or weak (causing negligible shear wave splitting) upper mantle anisotropy (e.g., Lynner & Long, 2013; Nowacki et al., 2010), so that accurate upper mantle corrections can be applied. For the case of a single layer of seismic anisotropy, a correction is applied to all waveforms by rotating and time shifting the horizontal components to remove the effect of shear wave splitting due to upper mantle seismic anisotropy (e.g., Lynner & Long, 2013), and the residual waveform should reflect the shear wave splitting due to seismic anisotropy in the lowermost mantle. Typically, long = running or permanent seismic stations are best suited for this type of analysis, as many SK(K)S splitting measurements with good backazimuthal coverage is needed to characterize the upper mantle shear wave splitting in detail. We investigated the station coverage in and around our study area, looking to identify stations with suitably simple upper mantle seismic anisotropy signatures and that measured core phases that sample the D″ layer beneath Siberia. We identified a single station, LVZ (Global Seismographic Network) in Lovozero, Russia (Figure 1), that is both suitably positioned to sample our study region and meets the criteria for the upper mantle shear wave splitting corrections.

To characterize the upper mantle shear wave splitting signal beneath the station LVZ, we measured the splitting of SK(K)S phases using three measurement techniques. The first, the multichannel method of Chevrot (2000), measures splitting intensity (a quantity related to the amplitude of the transverse component waveform, compared to the amplitude of the time derivative of the radial component). For a single layer of seismic anisotropy, the splitting intensity (*SI*) is related to the shear wave splitting parameters ($\phi, \delta t$) by $SI = \delta t * \sin\left(2\beta\right)$, where δt is delay time and β is the angle between the initial polarization direction (equivalent to the backazimuth for SK(K)S waves) and ϕ, the fast shear wave splitting direction (Chevrot, 2000). Therefore, we fit a $\sin\left(2\beta\right)$ curve to the splitting intensity data to obtain estimates of (ϕ, δt) due to upper mantle seismic anisotropy beneath the station. We also used the transverse component measurement method of Silver and Chan (1991), with an updated error formulation proposed by Walsh et al. (2013), and the rotation-correlation method (Bowman & Ando, 1987). Apparent shear wave splitting parameters estimated using these measurement methods are expected to vary with backazimuth for the case of multiple layers of seismic anisotropy (e.g., Silver & Savage, 1994) and such behavior can be used to diagnose complex seismic anisotropy beneath a station. We used an implementation of the SplitLab software (Wüstefeld et al., 2008) that uses all three methods; the splitting intensity measurements were incorporated in a software update described by Deng et al. (2017).

We measured SKS and SKKS phases across a range of backazimuths to obtain an estimate of shear wave splitting parameters due to upper mantle seismic anisotropy beneath station LVZ (Figure 2a). We applied

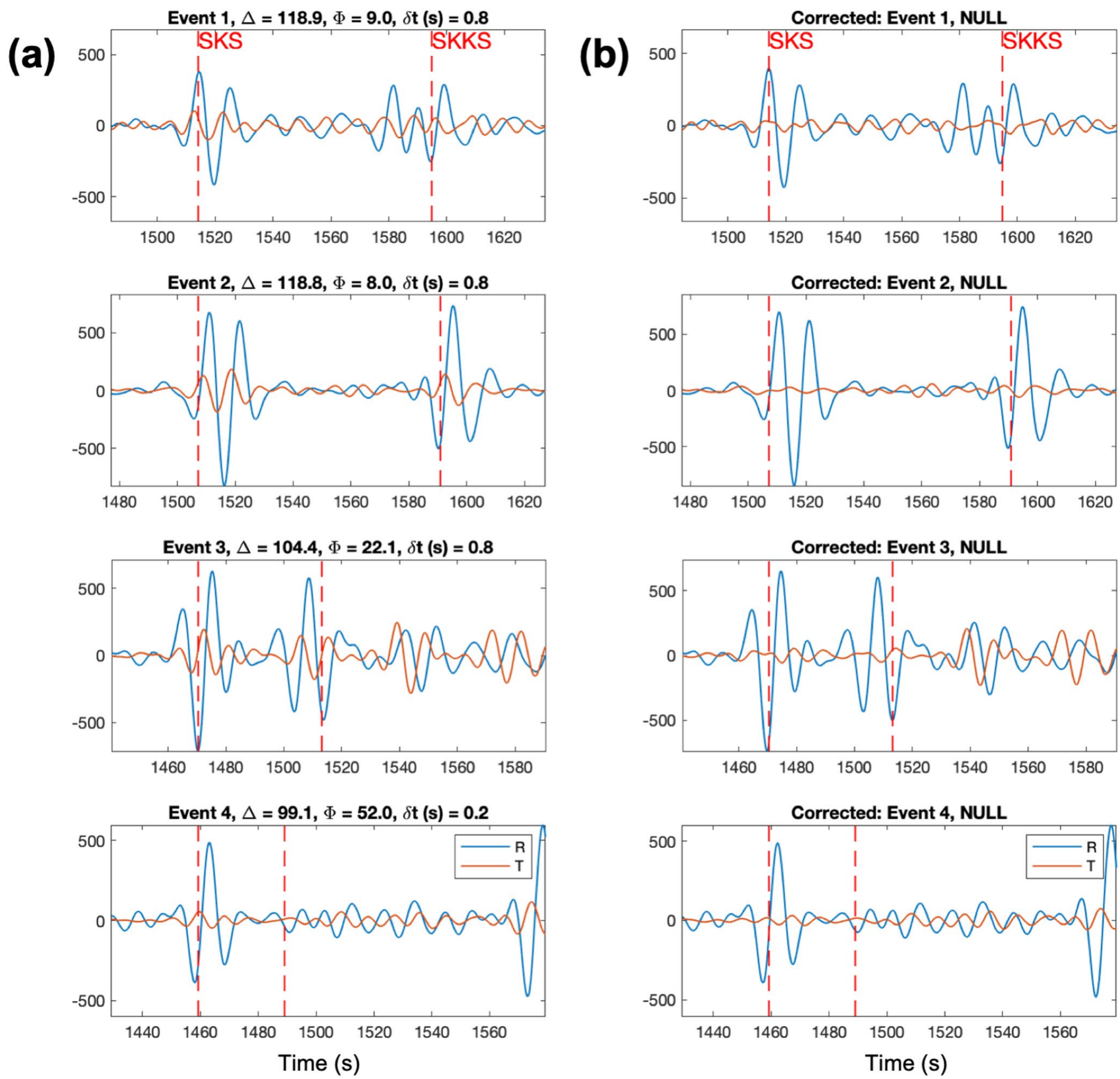

Figure 2. Example of SKS waveforms at station LVZ after filtering, including initial waveforms (a) and waveforms after correcting for the effect of upper mantle shear wave splitting (b). Radial components are shown in blue and transverse components in orange. We measured shear wave splitting for each of these SKS waveforms (both corrected and uncorrected; estimated fast directions in degrees and delay times in seconds are shown, along with the epicentral distance Δ); SKKS waveforms are also shown for comparison. Initial waveforms are normally split or null (e.g., Event 4), but after upper mantle corrections, most waveforms show little to no energy on the transverse component, resulting in a null measurement (marked as NULL).

a band-pass filter with corner periods of 8 and 25 s to all waveforms. To avoid inaccuracies potentially introduced by the effects of frequency dependent splitting (e.g., Eakin & Long, 2013), we use the same period band for all measurements. Seismograms were inspected manually for high signal-to-noise ratio (higher than five; any other values with an SNR <5 are automatically labeled poor quality) and good waveform clarity and were manually windowed for shear wave splitting analysis. We selected events of moment magnitude 5.5 and greater at epicentral distances between 90° and 122°. We obtained 256 high-quality measurements of SKS and SKKS measurements, as shown in Figure 3a. Splitting intensity estimates, plotted as a function of backazimuth, show a clear sinusoidal variation, with best-fitting shear wave splitting parameters

10.1029/2021GC009924

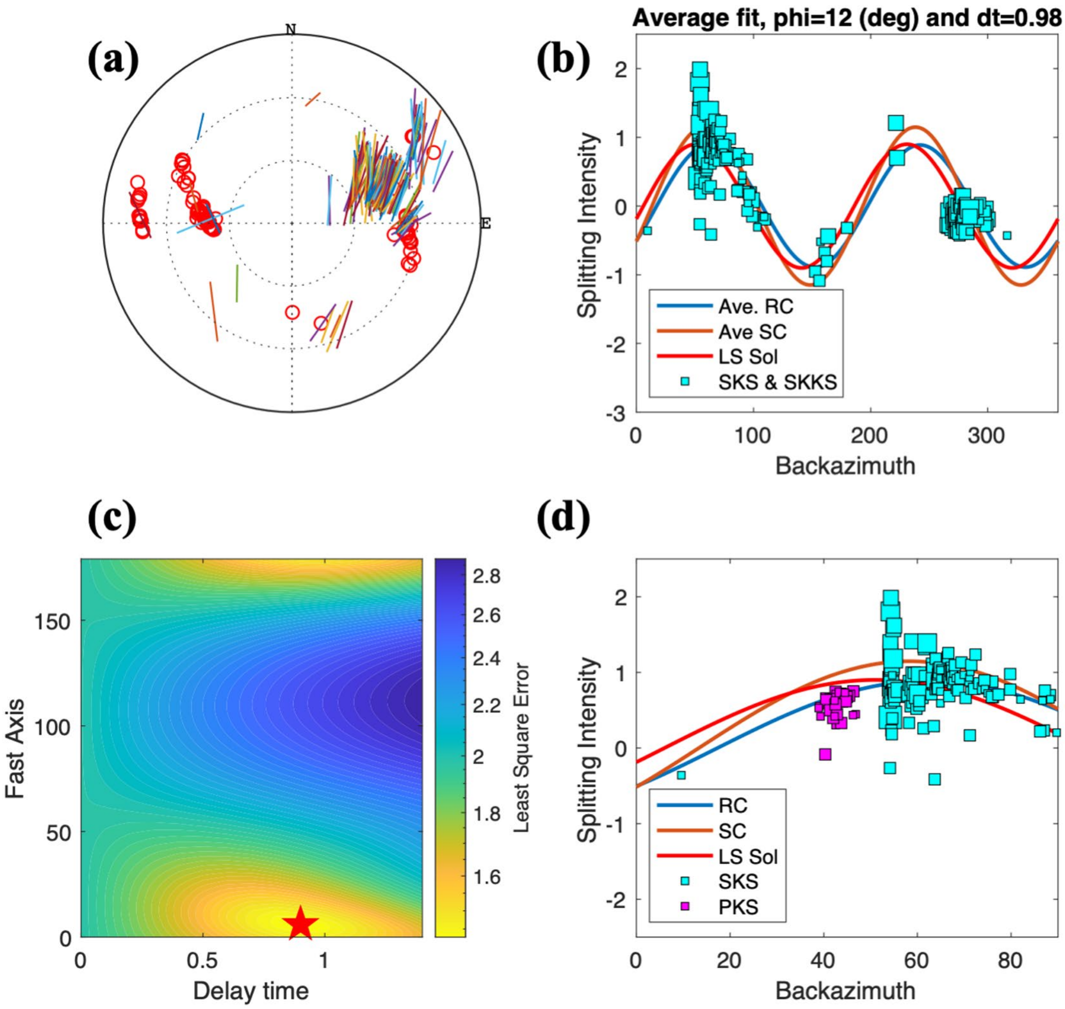

Figure 3. Estimates of SKS splitting due to upper mantle seismic anisotropy beneath station LVZ. (a) Stereo plot showing apparent SKS (and some SKKS) splits (sticks) and nulls (red circles) as a function of backazimuth, estimated using the rotation correlation method. (b) Splitting intensity measurements (cyan squares) of SKS and SKKS for the same phases measured in (a); symbol size represents error estimates. We also show three different estimates of shear wave splitting parameters derived from single-layer modeling, displayed as sin(2θ) curves (lines). Amplitudes and phases of sinusoids were derived from shear wave splitting parameters obtained by averaging all rotation-correlation measurements (Ave. RC–blue), by averaging all transverse component minimization measurements (Ave. SC–orange), and by fitting a sinusoid to the splitting intensity data using a minimized least squares fit (LS Sol–red). (c) Least squares error grid search for the best fitting fast axis direction (in degrees) and delay time (seconds) for the splitting intensity data in (b). Red star represents best fit solution. (d) Splitting intensity as a function of backazimuth for SKS/SKKS (cyan) and PKS (magenta) for a narrow backazimuthal window that contains the PKS data that samples our study region.

of $\phi = 12°$, $\delta t = 0.98$ s (Figure 3b). We also obtained complementary upper mantle shear wave splitting estimates via three different approaches: a grid search approach by solving for the minimum least squares error on the splitting intensity measurements by calculating a plausible range of fast directions and delay times (Figure 3c), averaging all transverse component minimization fast directions (Silver & Chan, 1991), and averaging all rotation-correlation fast directions (Bowman & Ando, 1987). Estimates of apparent shear wave splitting using the rotation-correlation method and transverse component minimization technique show little or no variability in apparent shear wave splitting with backazimuth, consistent with a single layer of seismic anisotropy. Furthermore, our estimates of shear wave splitting beneath LVZ is consistent with previously published work (Wüstefeld & Bokelmann, 2007).

To identify splitting of shear core-refracted phases due to lowermost mantle seismic anisotropy, we applied the upper mantle corrections to a set of selected waveforms that sample our study area and measured the residual shear wave splitting. An example of an upper mantle correction is shown in Figure 2b on SKS and SKKS waveforms. For this part of the analysis, we selected SKS-SKKS pairs at epicentral distances between 108° and 122° within our dataset (at these distances, both SKS and SKKS phases are often visible on the same seismogram (e.g., Niu & Perez, 2004) and SKS-SKKS splitting discrepancies can be detected).

We also measured other available core phases, notably PKS, which is a core phase similar to SKS and SKKS that is visible at distances from 125° to 145°. We measured PKS phases over a backazimuth range suitable to target our study region (Figure 3d). PKS phases have been commonly used for measuring shear wave splitting in the upper mantle in combination with SKS (e.g., Liu & Gao, 2013); they have similar upper mantle incidence angles and are often similar in their shear wave splitting parameters. SKS, SKKS, and PKS have inclination angles in the upper mantle that range from 5 to 9°, 11 to 13°, and 4 to 8°, respectively, at the distance ranges used in our study; therefore, the upper mantle should be sampled similarity by each phase. The correction and subsequent splitting measurement methods for PKS are the same as for SKS corrections, similar to making corrections for SKKS and S-ScS differential splitting (e.g., Lynner & Long, 2014; Wookey et al., 2005). We collected 34 PKS observations in a backazimuthal window that sample the same region of the lowermost mantle as the previously published observations.

3. Summary of Observations

3.1. Shear Wave Splitting Results

Our analysis of SKS, SKKS, SKiKS, and PKS phases that had been corrected for the effect of upper mantle seismic anisotropy revealed that for the most part SKS phases do not appear to experience shear wave splitting due to lowermost mantle seismic anisotropy, with 48 null (non-split) SKS phases that sample beneath Siberia (Figure 4). Put differently, nearly all the SKS splitting we measured was consistent with shear wave splitting due to upper mantle seismic anisotropy beneath stations LVZ. We did observe a single SKS phase, which sampled to the north of the bulk of the measurements, that had D″-associated shear wave splitting. We also measured a smaller number of SKKS ($n = 9$) and SKiKS ($n = 2$) measurements (Figure 2) that were mostly non-split by the lower mantle, with a very few exceptions (specifically a few SKKS phases, $n = 3$).

For PKS phases, we found clear and consistent evidence for splitting due to seismic anisotropy in the lowermost mantle (that is, shear wave splitting that could not be well explained by upper mantle seismic anisotropy beneath LVZ). We measured 34 PKS phases that sampled the lowermost mantle beneath our study region and for most of the individual waveforms, we measured relatively weak but resolvable shear wave splitting (with a few individual null measurements). We considered the possibility of contamination from the SKP arrival, which becomes separated from the PKS arrival as event depth increases. To evaluate the possible effects of phase contamination, we looked for variations in measured PKS splitting as a function of event depth, but did not identify any such variations, suggesting no effect of SKP on our measurements. Before estimating the shear wave splitting due to the lowermost mantle, we corrected each PKS waveform by using the SKS upper mantle modeling from Figure 3. There is some scatter in the observed PKS splitting measurements, as is typical for shear wave splitting studies (e.g., Asplet et al., 2020; Creasy et al., 2017; Deng et al., 2017; Grund & Ritter, 2020; Long, 2009; Lutz et al., 2020; Niu & Perez, 2004). Therefore, we stacked each PKS error surface (after upper mantle correction) using Stacksplit (Grund, 2017) and found best-fitting PKS splitting parameters (due to D″ seismic anisotropy) of $\phi = -85° \pm 10°$ ($\phi = -41°$ in ray-centered coordinates, using the convention of Wookey et al., 2005 and Nowacki and Wookey, 2010) and $\delta t = 0.4$ s $\pm$ 0.1 s (Figure 5). This energy stacking approach improves the quality of the measurements when all the phases sample the same region over a small back azimuthal window.

We incorporated this new PKS splitting measurement (Figure 1 and Table 1) in our modeling scheme, described below. Because the other phases (SKS and SKKS) showed some geographic variability in their D″-associated splitting behavior, with phases that sampled close to the volume of mantle sampled by PKS exhibiting splitting and phases that sample to the south exhibiting no D″-associated splitting (Figure 4), we did not include them in our modeling. Specifically, the volume of lowermost mantle sampled by the PKS phases is located near the crossing point for the ScS paths used in our joint modeling (Figure 1), while the

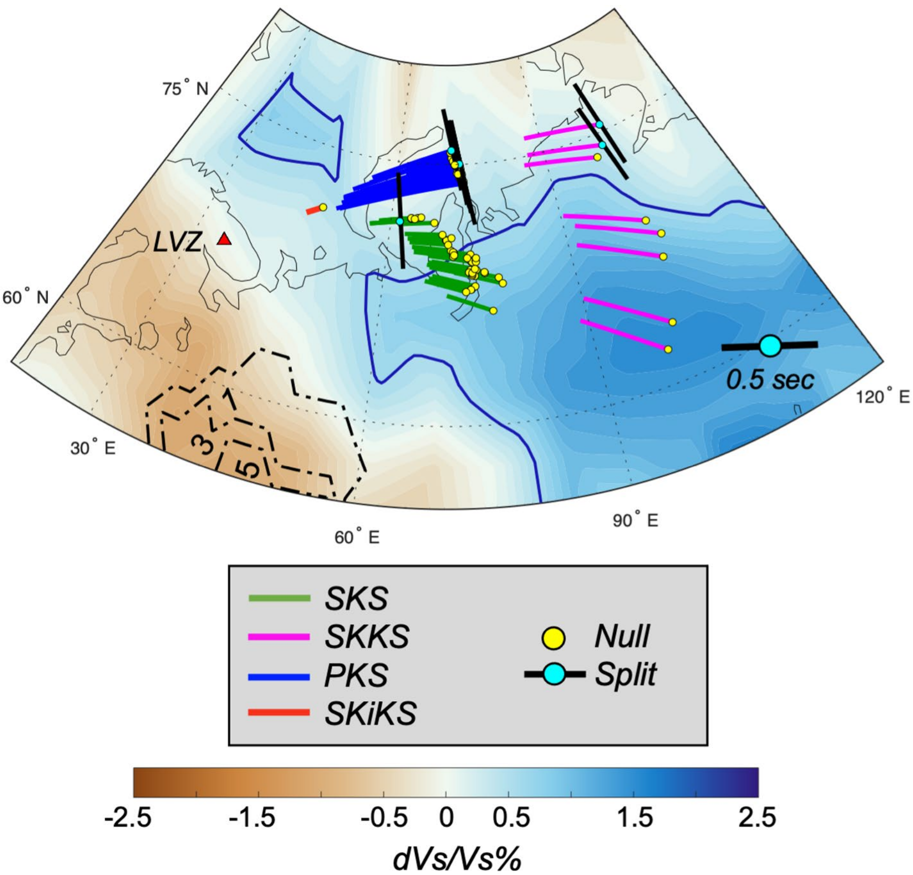

Figure 4. Summary of D″-associated splitting measurements made at station LVZ (red triangle). Map of all SKS (green), SKKS (magenta), PKS (blue), and SKiKS/SKIKS (purple) measurements beneath Siberia. Black sticks with light blue dots represent measurements of D″-associated splitting; bars are aligned with measured fast directions in the ray reference frame. Yellow dots denote null measurements (i.e., phases that show no contribution to shear wave splitting from D″ seismic anisotropy). Each dot is plotted at the pierce point of each corresponding phase as it exits the CMB. Colored lines show the length of each raypath within D″ (assuming a 250-km-thick layer). Background colors and plotting conventions are as in Figure 1.

volume of mantle sampled by most of the SKS and SKKS phases lies to the south of this region. Therefore, we did not include the SKS and SKKS phases in our modeling, and instead focused on the PKS phases as more geographically relevant.

We also incorporated the previously published differential S-ScS shear wave splitting data of Wookey and Kendall (2008), who measured D″-associated shear wave splitting beneath Siberia for two nearly perpendicular crossing raypaths. Each raypath exhibited different ScS splitting parameters, where the north-south and east-west paths have fast directions of $\phi = -87°$ and $\phi = -35°$ in the ray-centered reference frame and delay times of $\delta t = 2.7$ s and $\delta t = 1.5$ s, respectively (Figure 1 and Table 1). The nearly north-south path used events in the Hindu-Kush region and stacked S and ScS waveforms collected at the POLARIS network in the Northwest Territories of Canada. The east-west path used events from the Kuril Arc that were recorded at the German Regional Seismic Network (GRSN).

3.2. Reflection Polarity Measurements

Thomas et al. (2011) used data from several seismic arrays to construct vespagrams or slowness stacks (e.g., Rost & Thomas, 2002) to identify weak reflections from the D″ discontinuity beneath Siberia (Figure 1 and Table 1). They obtained measurements of both PdP and SdS phases, which arrive as precursors to the main PcP and ScS phases, respectively. Thomas and Kendall (2002) and Thomas and Weber (1997) also

10.1029/2021GC009924

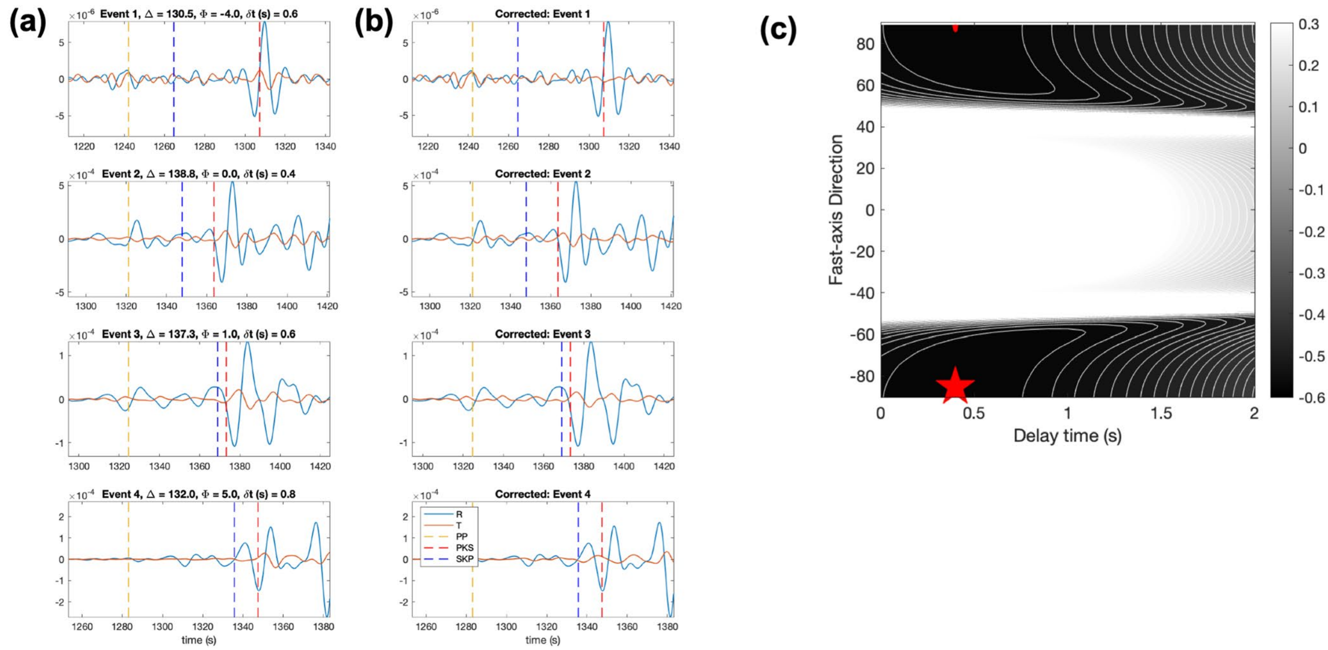

Figure 5. Example of filtered PKS waveforms, including initial waveforms (a) and waveforms after correction for the effect of upper mantle shear wave splitting (b). Radial components are shown in blue and transverse components in orange. Dashed vertical lines indicate estimated arrival times for phases, as indicated in the legend; PKS arrival times are marked with dashed red lines. We measured splitting for each of these PKS waveforms (both corrected and uncorrected; estimated fast directions in degrees and delay times in seconds are shown, along with the epicentral distance Δ). (c) Stacked error surfaces for the best-fitting D″-associated shear wave splitting parameters for the PKS phases shown in (b). Stack includes 34 individual error surfaces, as estimated using the rotation correlation measurement method, for PKS phases. Red star represents best solution. The 95% confidence interval is covered by red star. Grayscale background is the average stack for each error surface for the RC method.

made several reflection polarity measurements over a set of paths that sample beneath Siberia. Taken together, these previous studies provide five unique PdP/SdS polarity measurements (when individual measurements with similar paths are averaged), with three PdP and two SdS reflections. The previous studies identified positive PdP and SdS reflections (positive measurements are such that the PdP/SdS reflection has

Table 1
Summary of D″ Seismic Anisotropy Observations Beneath Siberia, Including All Measurements Used in the Modeling in This Study

Measurements

Shear wave splitting

Station/Array	Reference	Phase	Azimuth (°)	Inclination (°)	φ (°)	δt (s)
POLARIS (Canada)	WK	ScS	1.5	20	87	2.7
GRSN (Germany)	WK	ScS	262	20	35	1.5
LVZ	This study	PKS	255	60–68	−41	0.4

Reflection polarity

Array	Reference	Phase	Azimuth (°)	Distance (°)	Polarity
POLARIS (Canada)	TH	PdP/SdS	1.5	78	Positive
GRSN (Germany)	TH	PdP/SdS	262	75	Positive
DAG, HJO (Greenland)	TH	PdP	324	75	Negative

Note. For both types of measurements, we include the station or array, seismic phase, and azimuth of average raypath in D″. For shear wave splitting measurements, we include inclination from the horizontal of average raypath in D″, average fast shear wave splitting direction (in a ray-centered coordinate system), and average delay time. For reflection measurements, we report the average distance and polarity of the relevant SdS or PdP phases. For previously published measurements, we include the reference: WK, Wookey and Kendall (2008); TH, Thomas et al. (2011).

the same polarity as the corresponding P/S and PcP/ScS phase) measured at stations of the GRSN and GRF (Gräfenberg) arrays in Germany from events in the northwest Pacific Ocean. A crossing path of positive PdP and SdS was also measured by Thomas et al. (2011) using data from events in the Hindu Kush region recorded at the POLARIS array in Canada. A third crossing path was measured (only for PdP) at two stations in Greenland (stations HJO and DAG) for events from China; this observation yielded a negative polarity observation and was slightly offset from the two perpendicular paths. Our use of stacking and emphasis on deep events (which are often impulsive) helps to avoid potential complications due to complex source time functions. This set of five unique PdP/SdS reflections was used in our joint modeling, along with the PKS and ScS splitting measurements described in Section 3.1.

4. Joint Modeling of Seismic Anisotropy Observations

4.1. Modeling Method and Approach

To identify plausible mechanisms for, and geometries of, D″ seismic anisotropy beneath Siberia that are consistent with observations, we implemented a modeling scheme that is based on the findings of Creasy et al. (2019) and adapted from the approach used by Ford et al. (2015) and Creasy et al. (2017). To summarize, this modeling process is based on rotating each elastic tensor model over every possible orientation (5° steps) and calculating (in a ray theoretical framework) the predicted shear wave splitting parameters (using the Christoffel equation) and reflection polarities (calculating the reflection coefficients, see Pisconti et al., 2019) for each raypath geometry in the combined data set. We then compare the observations to the predicted values. We eliminate a particular candidate orientation (for each elastic tensor model) if the predicted reflection polarity does not match the observed polarities. For shear wave splitting measurements, if the difference in fast directions between observed and predicted data differ by more than 20° (based on typical errors of shear wave splitting measurements; see Ford et al., 2015), we eliminate the model's candidate orientation as inconsistent with the data. If we find that no orientation can fit the shear wave splitting measurements and reflection polarities simultaneously, we can eliminate that elastic tensor model as a plausible description of seismic anisotropy in our study region.

We tested 10 possible scenarios based on the most likely mechanisms for D″ seismic anisotropy: CPO of post-perovskite, bridgmanite, or ferropericlase. We did not consider a partial melt SPO model since SPO models have been shown to predict insufficient changes in reflections to explain observed PdP/SdS polarity data (Pisconti et al., 2019). These 10 scenarios (labeled A–J; shown in Figure 6 and Tables 2 and 3) were based on previously published models that incorporated calculations of reflectivity predictions for PdP and SdS phases (Thomas et al., 2011), as well as models that were considered in the synthetic modeling study of Creasy et al. (2019). We considered two different types of elastic tensors: those based on estimates of single-crystal elasticity and those derived from visco-plastic self-consistent (VPSC; Lebensohn & Tomé, 1994) modeling. The first set of models (Models A–F) were based on single-crystal elastic tensors; we assumed that 12% of the crystals were aligned and obtained a bulk elastic tensor by mixing them linearly with an isotropic equivalent (This approach is described in more detail in Thomas et al. [2011] and Creasy et al. [2019]). The second set of models (Models G–J) came from a published library of elastic tensors for lowermost mantle seismic anisotropy (Creasy et al., 2020) and were derived from VPSC modeling of post-perovskite deformed under simple shear with 100% strain, with various assumptions about the dominant slip systems.

Models A–D represent two post-perovskite scenarios with different isotropic layers (with different seismic velocities) above the seismic anisotropic layer (Table 2). The properties of the material overlying the seismic anisotropic layer do not affect the predicted shear wave splitting, but they do affect the predictions of reflection polarities (Thomas et al., 2011). We used two different scenarios for the overlying isotropic layer in our work based on two different values for isotropic wave speeds (Scenario 1: Vp = 14.01 km/s and Vs = 7.45 km/s and Scenario 2: Vp = 14.07 km/s and Vs = 7.33 km/s). These values for Vp and Vs reflect the expected differences between a bridgmanite (Scenario 1) versus post-perovskite (Scenario 2) mineralogy for the overlying layer. These different scenarios reflect the possibilities that the onset of seismic anisotropy in the D″ layer could be due to either to a phase transition (from bridgmanite to post-perovskite) or to other factors, such as a transition from diffusion to dislocation creep at the base of the mantle.

10.1029/2021GC009924

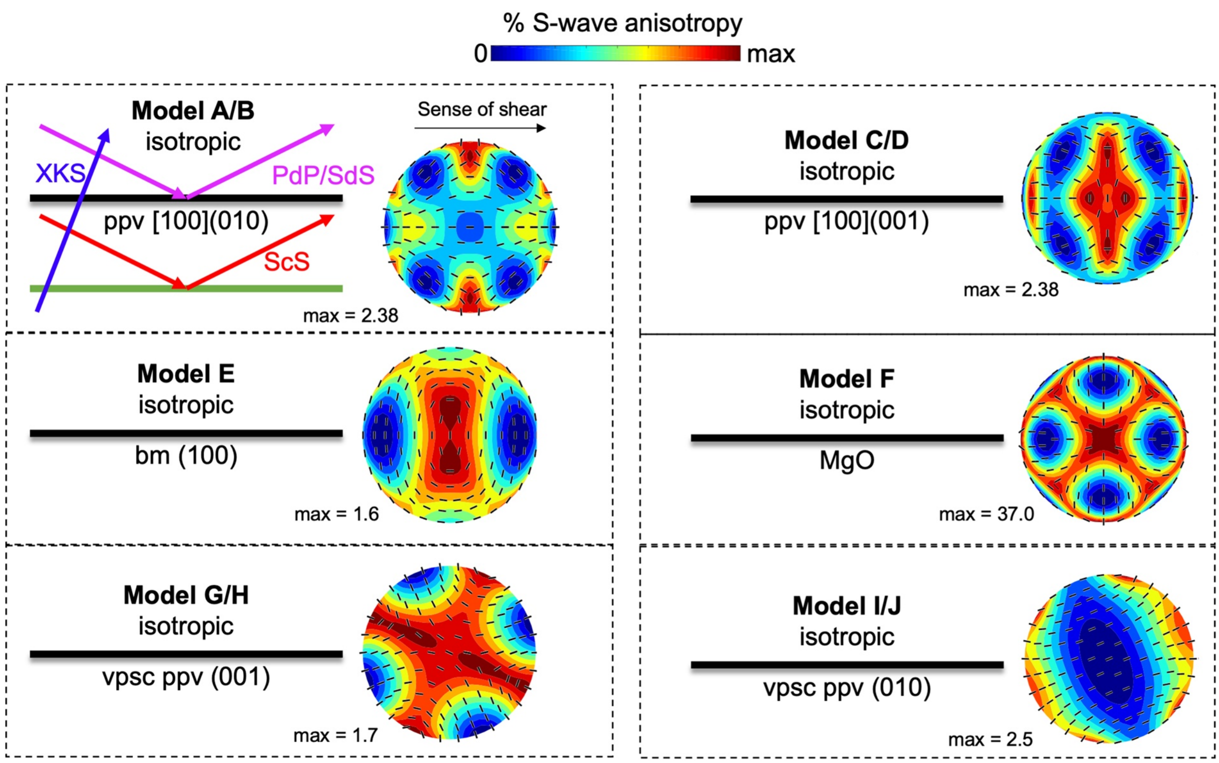

Figure 6. Schematic diagram of models tested in this study. Models A-D invoke post-perovskite as the source of seismic anisotropy with two different dominant slip systems: Models A/B – [100](010) and Models C/D – [100](001). Models A/B and C/D are differentiated by the velocities in the isotropic layer, as described in the text. Model E invokes bridgmanite and Model F invokes ferropericlase. Models G–J are VPSC-based models of post-perovskite texture with two different dominant slip systems: Models G/H – (001) and Models I/J – (010). Again, models I/J are differentiated by the velocities in the isotropic layer. Each model includes an isotropic top layer and a seismic anisotropic bottom layer; the seismic anisotropic properties of the bottom layer are represented with stereo plots of predicted S-wave anisotropy looking down from above the shear plane. Numbers at the base of each stereo plot show the maximum value of shear wave anisotropy (in percent) for that elasticity model. In the cartoon for Model A/B, we illustrate the phases used in this study and their approximate propagation paths through the model.

For Models A–D, we used the same underlying elastic constants to describe the seismic anisotropic medium (single-crystal elastic constants for post-perovskite, from the work of Wentzcovitch et al., 2006). However, when we interpret the seismic anisotropy in terms of deformation geometry, we make a different set of assumptions. Models A and B assume a dominant slip system of [100](010), as has been suggested by previous work (Kubo et al., 2008; Miyagi et al., 2008; Yamazaki et al., 2006); these two models are different from each other in the assumptions made about the overlying isotropic layer. Models C and D assume a dominant slip system of [100](001), as previously suggested (Hirose et al., 2010; Miyagi et al., 2010).

For Model E, we used single-crystal elastic constants appropriate for bridgmanite (Stackhouse et al., 2005); when interpreting our models in terms of deformation geometry, we assumed dominant slip on [010](100) (Couper et al., 2020; Tsujino et al., 2016). Model F invoked ferropericlase as the cause for lowermost mantle seismic anisotropy, using single-crystal elastic constants from Karki et al. (1999) and assuming a dominant slip system [100](001). This assumption is based on experimental work that has suggested that the [100] or {100} slip direction is preferred for the lowermost mantle (Amodeo et al., 2012; Cordier et al., 2012; Girard et al., 2012; Immoor et al., 2018). Models G–J consider CPO of post-perovskite, similar to Models A–D, but instead of elastic tensors based on single-crystal elasticity we instead use tensors calculated using VPSC for the simple shear of post-perovskite with 100% strain, from Creasy et al. (2020). In order to calculate the reflection polarities for PdP and SdS for Models G–J, we removed the lower symmetry monoclinic and triclinic components (~0.2% of each elastic tensor) from the VPSC-based elastic tensors using the decomposition method of Browaeys and Chevrot (2004), as implemented in the MSAT toolkit (Walker & Wookey, 2012).

We predicted reflection polarities and shear wave splitting parameters for paths corresponding to the seismic observations shows in Figure 1 for the suite of models we considered, and compared them to observations

Table 2
All Single-Crystal Models Tested for ppv (Post-Perovskite), bm (Bridgmanite), and MgO (Ferropericlase)

Model	*Isotropic Layer*	*Anisotropic Layer*	*Anisotropic Layer Elastic Tensor*					
Model A	Layer 1	ppv [100](010)						
Vp	14.00	14.01	1055	443	451	0	0	0
Vs	7.45	7.45	443	1053	455	0	0	0
Density	5297	5302	451	455	1024	0	0	0
Model B	Layer 2	ppv [100](010)	0	0	0	290	0	0
Vp	14.07	14.01	0	0	0	0	301	0
Vs	7.33	7.45	0	0	0	0	0	287
Density	5232	5302						
Model C	Layer 1	ppv [100](001)						
Vp	14.00	14.01	1055	451	443	0	0	0
Vs	7.45	7.45	451	1024	455	0	0	0
Density	5297	5302	443	455	1053	0	0	0
Model D	Layer 2	ppv [100](001)	0	0	0	290	0	0
Vp	14.07	14.01	0	0	0	0	287	0
Vs	7.33	7.45	0	0	0	0	0	301
Density	5297	5302						
Model E	Isotropic bm	bm [010](100)	1042	475	483	0	0	0
			475	1039	470	0	0	0
Vp	14.07	14.07	483	470	1022	0	0	0
Vs	7.33	7.33	0	0	0	281	0	0
			0	0	0	0	280	0
Density	5297	5237	0	0	0	0	0	287
Model F	Isotropic fp	fp [100](001)	1239	299	299	0	0	0
			299	1239	299	0	0	0
Vp	14.27	14.27	299	299	1239	0	0	0
			0	0	0	202	0	0
Vs	7.84	7.84	0	0	0	0	202	0
Density	5035	5035	0	0	0	0	0	202

Note. Each model is described by the top isotropic and bottom seismic anisotropic layer, with Vp and Vs in km/s and density in kg/m^3. Each seismic anisotropic layer is noted with the anisotropic mineral and dominant slip system, as well as its elastic tensor, with elastic coefficients in GPa.

following the method of Ford et al. (2015). We assumed that the seismic anisotropic structure is laterally homogenous within our region of study, and thus that each of the individual raypaths is sampling the same seismic anisotropy. For each group of raypaths, we calculated an average straight-line approximate raypath through D″, identifying a representative azimuth and inclination for each group of phases, as outlined in Table 1. We used a previous estimate of the thickness of the D″ layer beneath Siberia of 300 km (Weber & Davis, 1990). For ScS, we assumed horizontal propagation through D″ (following the approach of previous studies, e.g., Ford et al., 2015; Creasy et al., 2017; Nowacki et al., 2010), although in the real Earth propagation angles can vary from the horizontal up to ∼10°–20°. We used TauP (Crotwell et al., 1999) with the PREM velocity model (Dziewonski & Anderson, 1981) to model raypath geometries though the D″ layer.

Table 3
All ppv VPSC (Visco-Plastic Self-Consistent) Models Tested for Simple Shear Scenarios Using the Single Crystal of ppv at 135 GPa and 3,000 K (Stackhouse et al., 2005)

Model	***Isotropic Layer***	***Anisotropic Layer***	***Anisotropic Layer Elastic Tensor***					
Model G	Layer 1	Vpsc ppv (001)						
Vp	14.00	13.97	1022	445	430	-0.1	-0.8	15.4
Vs	7.45	7.50	445	1057	459	-0.1	-0.3	4.5
Density	5297	5336	430	459	1048	0.1	-0.6	10.9
Model H	Layer 2	Vpsc ppv (001)	-0.1	-0.1	0.1	302	-0.5	0.1
Vp	14.07	13.97	-0.8	-0.3	-0.6	-0.5	303	0.3
Vs	7.33	7.50	15.4	4.5	10.9	0.1	0.3	296
Density	5297	5336						
Model I	Layer 1	Vpsc ppv (010)						
Vp	14.00	13.97	1060	440	441	-0.3	0.4	5.2
Vs	7.45	7.50	440	1020	442	0.2	0	14.7
Density	5297	5336	441	442	1046	-0.1	0.7	-0.6
Model J	Layer 2	Vpsc ppv (010)	-0.3	0.2	-0.1	294	6.1	0.6
Vp	14.07	13.97	0.4	0	0.7	6.1	306	-0.2
Vs	7.33	7.50	5.2	14.7	-0.6	0.6	-0.2	300
Density	5297	5336						

We transformed the shear wave splitting parameters into a ray-centered coordinate system for our analysis, following Nowacki et al. (2010).

For PKS phases, our analysis considered the fact that there is a triplication of PKS at the CMB by considering the full range of inclination angles for all branches of the triplication (because it can be difficult to confidently identify which branch of the triplication an individual PKS arrival corresponds to). We considered inclination angles from the horizontal between 60° and 70° in the D″ layer and modeled the full range of possible inclinations. We analyzed whether there were strong variations in predicted fast shear wave splitting directions across this range; if no strong variations were present, and if the average predicted fast shear wave splitting direction fit the observation, then we judged that the model under consideration fit the data.

For each model (A–J) under consideration, we tested all possible orientations of the tensor by rotating each candidate elastic tensor in 5° increments around each of the three rotation axes, following Ford et al. (2015) and Creasy et al. (2017, 2019). For each candidate orientation, we predicted shear wave splitting parameters for each group of ScS and PKS raypaths by solving the Christoffel equation using MSAT (Walker & Wookey, 2012) and predicted SdS and/or PdP reflection polarities using the approach of Guest and Kendall (1993). This approach, which was also used by Thomas et al. (2011) and Pisconti et al. (2019), calculates reflection coefficients (and thus reflection polarities) at the interface between an isotropic and seismic anisotropic layer based on the velocity differences as a function of azimuth and epicentral distance. Implicit in this approach is the assumption that the PdP/SdS phases result from a discontinuity that is sharp enough to cause reflections and is associated with a mineralogical phase change, a change in seismic anisotropy, or a combination.

For reflection polarities, the consideration of whether the model prediction fit the data was straightforward, and we discarded all candidate models/orientations which incorrectly predicted any of the reflection polarity measurements. We also discarded each candidate model/orientation for which there was a difference of more than 20° between the predicted and observed fast shear wave splitting directions for any of the ScS or PKS splitting paths (following Ford et al., 2015). We did not discard any models based on differences between observed and predicted delay times, as delay time observations are generally less well constrained than fast shear wave splitting orientations. Furthermore, delay times are difficult to predict from a modeling point of view since they depend on assumptions made about the layer thickness, and the strength of seismic anisotropy may depend on the amount of strain (which is poorly known). For further discussion on the difficulty of modeling delay times, see Ford et al., 2015 and Creasy et al., 2017. Therefore, an acceptable model means that at least one orientation of the elastic tensor correctly predicts all polarity measurements and all shear wave splitting measurements (ScS and PKS) within the misfit cutoff. For all acceptable models, we calculated a total misfit value for the splitting observations based on a residual sum of squares approach, again following Ford et al. (2015). This misfit calculation used both the fast shear wave splitting directions and the delay times, weighted equally.

4.2. Modeling Results

Our key modeling results are shown in Figure 7, which illustrates the modeling using various combinations of data for Model A, and illustrates the best-fitting orientations of the shear direction and shear plane for the three most successful models we considered (Models A, C, and E). Figure 7a illustrates how each individual dataset (reflection polarities, ScS splitting, and PKS splitting) constrains the possible orientations of the post-perovskite elastic tensor, alone and in various combinations. For Model A, the reflection polarity observations by themselves are very efficient at constraining possible slip directions that are oriented either northeast-southwest or northwest-southeast (Figure 7a), similar to the findings of Thomas et al. (2011). When the ScS splitting observations (Wookey & Kendall, 2008) are considered in isolation (Figure 7a), we identify a range of permissible solutions over a range of azimuths and inclinations, with possible slip directions oriented mostly to the south. The addition of PKS splitting to the ScS dataset further tightens the range of acceptable models, when compared to the range derived from ScS data alone. Lastly, by combining the ScS and PKS splitting and reflection data and interpreting them jointly, we obtain a narrow range of acceptable solutions, each of which involve a shear direction toward the southwest.

As a side note, these acceptable solutions also generally predict weak or minimal splitting of SKS phases for the propagation direction of SKS measured at station LVZ (Figure 4), which is consistent with the null SKS observations that sample just to the south of our study region. There are challenges to fully incorporating null measurements in our framework because of the relatively large uncertainties in delay time measurements. There are several ways to produce a null measurement in the Earth (the material is isotropic; anisotropy is present, but the initial polarization direction aligns with a fast or slow direction of the medium; anisotropy is present, but the degree of splitting is weak and cannot be reliably differentiated from a true null measurement).

We applied our modeling procedure for the full range of models shown in Figure 6; full results for each model (similar to what is shown in Figure 7 for Model A) are shown in Figures S1–S8 and Table S1 in Supporting Information S1. We found that for many of the models we considered, there are no possible orientations that can fit all the data simultaneously, although there are often orientations that can fit a subset of the data (Figures S1–S8 in Supporting Information S1). In these cases, we find that each subset of data identifies different plausible orientations of the elastic tensor, and there is no overlap with the plausible orientations identified for other subsets of data. We found that in general, for almost every model it is possible to find orientations that fit the shear wave splitting measurements alone, but the reflection measurements are generally difficult to fit. Specifically, the reflection measurements are only consistent with Models A, B, and C (post-perovskite single-crystal), Model E (bridgmanite single-crystal), and Models G and I (post-perovskite VPSC). We found that there are only three models that provided a satisfactory fit to all observations: Model A, described above, Model C (post-perovskite), and Model E (bridgmanite), and for each of these models, there was a narrow range of plausible seismic anisotropy orientations that could fit the data. Figure 7b illustrates the best-fitting orientation solution (inferred shear direction and shear plane) for each of these three models, discussed further below. Because Models A and C are similar (each based on single-crystal elastic tensors for post-perovskite, and each invoking [100] as the dominant slip direction, although with

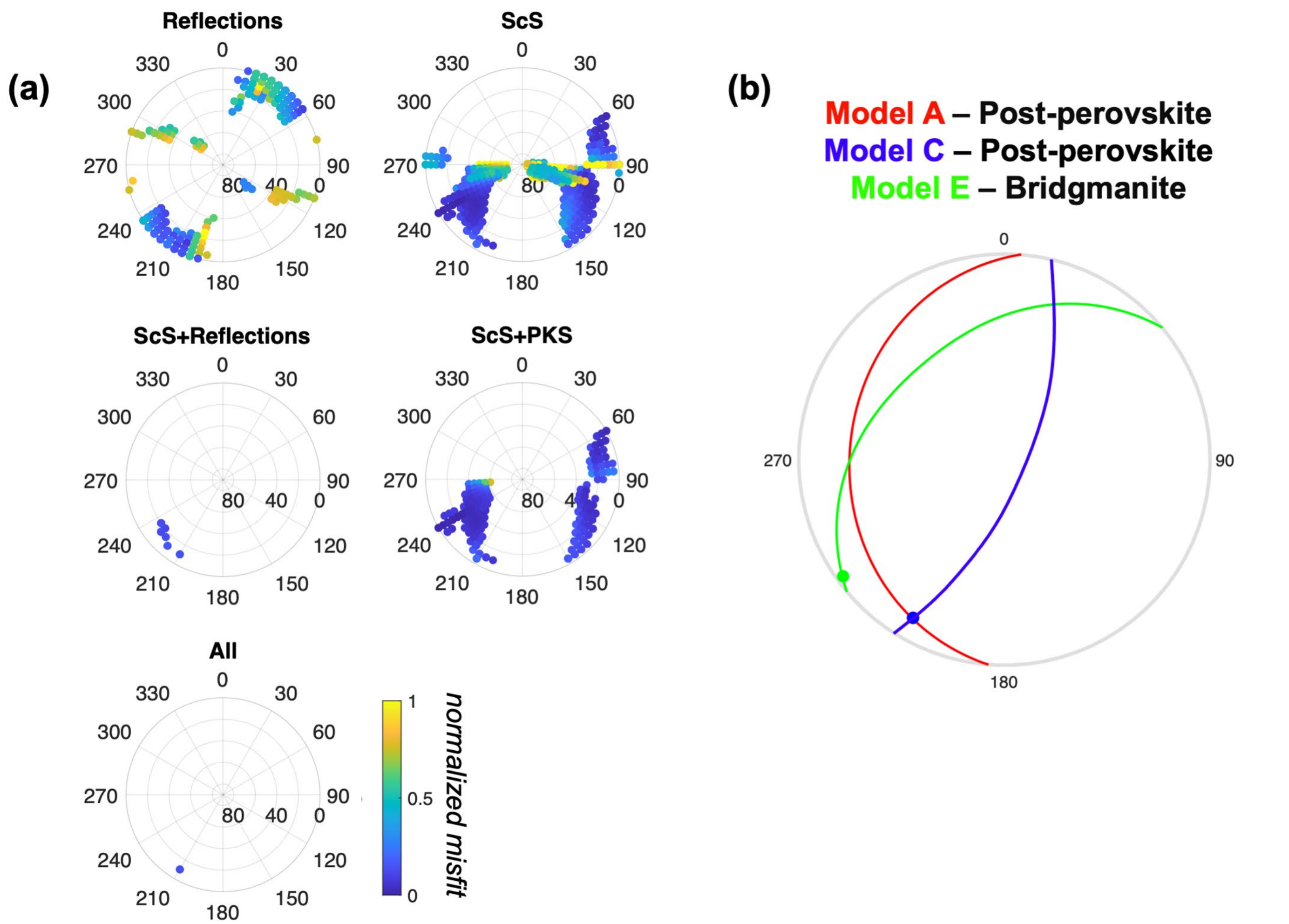

Figure 7. Modeling results for the successful models (Models A, C, and E.) (a) Illustration of how the best-fitting shear direction is constrained by various combinations of observations (our modeling also constrains the shear plane orientation, not shown in panel a). We show stereographic plots showing all permissible shear directions for Model A as constrained only by reflection polarity observations (top left, where color represents misfit of shear wave splitting measurements), only by ScS splitting (top right), a combination of only the ScS splitting and reflection polarities (middle left), a combination of ScS and PKS splitting (middle right) and combining all data (bottom left). Circles represent individual orientations; for panels that include shear wave splitting data, the colors represent total misfit for shear wave splitting observations for each orientation, as shown with the color bar. (b) Best-fitting deformation geometry (shear direction, squares; shear planes, lines) for Models A, C, and E. Note that the best-fitting shear directions for models A and C are nearly identical, except the shear plane differs.

different dominant shear planes), it is not surprising that they both provide good fits to the data. For all of the VPSC-based models and for the ferropericlase model (Model D), we found that there are no orientations that can reproduce all of the observations. Using only the reflection polarity measurements, we could find an acceptable orientation that fit the observations for almost all the models, except for Model D (ppv) and the VPSC-based models with Vs = 7.3 km/s for the isotropic upper layer (Models H and J).

Using only the shear wave splitting observations, we found that all the models can fit the data at some orientation except for Models I and J (both involve VPSC-based post-perovskite tensors with (010) as the dominant slip plane). When we considered only the previously published data (ScS splitting and reflections), we found that two of the VPSC-based models have orientations that successfully fit the data (Models G and I, each of which have the faster isotropic upper layer of Vs = 7.5 km/s). However, these particular models/orientations are not consistent with the new PKS observations documented in this study.

For the three most successful models (A, C, and E), we identified a best-fitting deformation geometry (shear direction and slip plane; Figure 7b). For Model A, the best-fitting direction for the [100] crystal axis (assumed to be the shear direction) is nearly horizontal (inclined 10° ± 5° from the horizontal) and oriented to either the southwest (azimuth of 210° ± 5°) or to the northeast (we cannot distinguish between these two possibilities, because there is a 180° ambiguity in the interpretation of the direction). Estimated error bars are based on our full suite of modeling results, since we test orientations using a series of rotations every 5°. For Model A, the best-fitting shear plane (oriented such that the [010] crystal axis is aligned with the shear plane normal) dips toward the east at 23° ± 5°. For Model C, the best-fitting inferred shear direction (that is, the orientation of the [100] crystal axis) is the same as for Model A (210° ± 5°), but the shear plane (corresponding to the direction of the [001] axis) is nearly vertical (dipping at 70° ± 5°). For Model E, which invokes aligned bridgmanite as the mechanism for seismic anisotropy, the shear direction ([010] crystal axis) is also oriented to the southwest (azimuth of 235° ± 5°) or, equivalently, to the northeast; the shear plane is dipping at an angle of 45° ± 5°. Each of these three models suggest similar shear directions, although the shear plane orientations vary from nearly horizontal to nearly vertical.

5. Discussion

The modeling work presented here illustrates the power of the approach proposed by Creasy et al. (2019) and Pisconti et al. (2019), in which data from co-located shear wave splitting and reflection polarity measurements are used to provide tighter constraints on D″ seismic anisotropy than would be available using a single data type. While Creasy et al. (2019) relied purely on synthetic modeling, here we show that the approach of combining multiple data types, for body waves propagating over multiple azimuths, can be successful using actual data. Previous studies of lowermost mantle seismic anisotropy beneath Siberia (Thomas et al., 2011; Wookey & Kendall, 2008) suggested that the incorporation of additional observations in the region could narrow the range of possible models for seismic anisotropy, and we have validated this idea here.

We identified three anisotropy scenarios that successfully reproduced the reflection polarity and shear wave splitting observations considered in this paper. Two of these scenarios (Models A and C) invoke the CPO of single-crystal post-perovskite as the mechanism for D″ anisotropy. (Models A and C are in a sense the same model, but because Model A invokes (010) as the dominant shear plane, and Model C invokes (001) as the dominant shear plane, they imply slightly different deformation geometries.) Models A and C have similar isotropic velocity contrasts across the seismic discontinuity as well. Models B and D, however, which are different from Models A and C only in that they invoke a different set of isotropic velocities above the discontinuity, do not have any orientations that agree with our polarity measurements or fall within our misfit cutoff for the shear wave splitting measurements. Model E, in contrast, invokes the CPO of bridgmanite. Therefore, our observations do not definitively favor one scenario (bridgmanite vs. post-perovskite) over another; either is compatible with the data. Each of the three successful models considered in this study suggests a similar shear direction; therefore, we consider the implications of lowermost flow toward either the south-southwest or the north-northeast in the geodynamic context of our study region (Figure 8).

Our study region beneath Siberia is notable for the presence of a number of slab fragments in the mid-to-lower mantle, known as a slab graveyard (Golonka et al., 2003; Stampfli & Borel, 2004; van der Meer et al., 2010, 2018; Van der Voo et al., 1999). Specifically, slab remnants likely present in our study area include the Mongol-Kazakh/Okhotsk (MO) slab at ∼2,850 km depth, just above the CMB, and the Komsomolets slab (Km) (∼2,200 km depth). Furthermore, our dataset samples just to the north of the Perm Anomaly (Lekic et al., 2012), a mesoscale feature that exhibits consistent low shear velocities in global tomography models. This dataset is also northwest of a previously mapped ultra-low velocity zone (ULVZ; Ross et al., 2004) with an approximate thickness of 8 km, while our observations likely do not sample this feature directly, we do note its proximity.

Paleogeographic reconstructions suggest that both the Mongol-Kazakh/Okhotsk and the Komsomolets slabs have been transported to the west (relative to surface features) during the time they have sunk through the mantle. Specifically, Fritzell et al. (2016) and Shephard et al. (2014) have suggested, based on global flow models that incorporate constraints from plate reconstructions, that the MO and Km slab remnants have migrated to the west-northwest over time.

The exact relationships (geographical and physical) between the slab remnants and the Perm anomaly remain unclear, but several previous studies (e.g., Bower et al., 2013; Flament et al., 2017; Hassan et al., 2015;

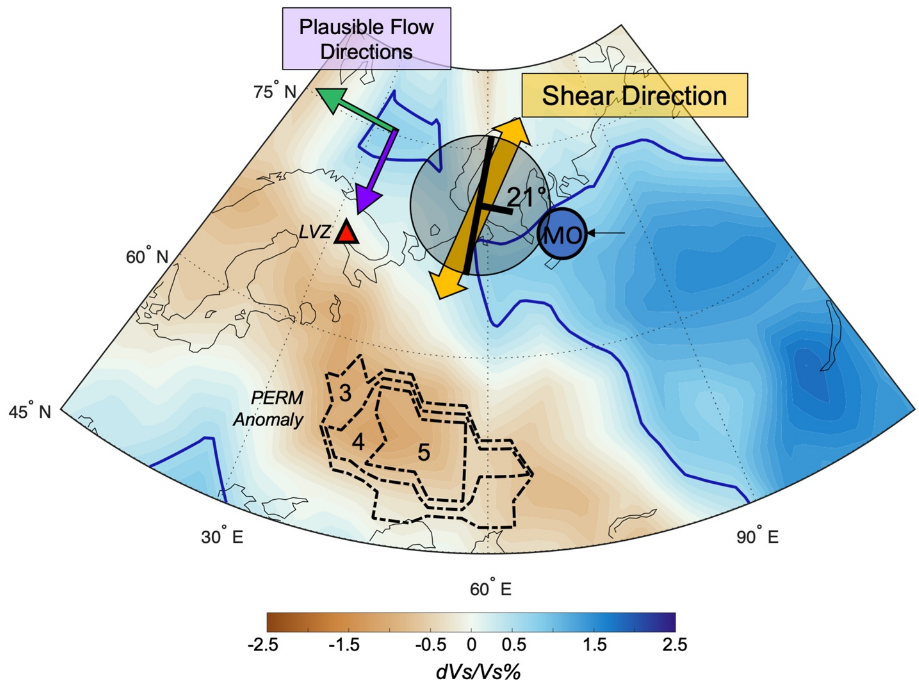

Figure 8. Schematic diagram showing the best shear direction (yellow arrow) and shear plane (black) for Model A, which invokes post-perovskite with a dominant slip system of [100](010) as the mechanism for lowermost mantle seismic anisotropy. The approximate present location of the Mongol-Okhotsk slab is shown as a blue circle (van der Meer et al., 2018). The black arrow indicates the direction in which the slab has been transported (van der Meer et al., 2018). Background colors and plotting conventions are as in Figure 1. The green and purple arrows represent the modeled flow direction at ~200 km above the core-mantle boundary for two different geodynamic models (TX2008 model of Forte et al. (2015) and a selected model from Flament (2019), respectively).

McNamara & Zhong, 2005) have explored whether past episodes of subduction may have played a role in creating and/or maintaining the Perm anomaly. The Perm anomaly has been shown to be similar in composition and dynamics to the Large Low Shear Velocity Provinces (LLSPVs), suggesting that LLSVPs and the Perm anomaly are in some ways analogous. Subducting slabs are thought to play a role in controlling the distribution of LLSVP material. Previous studies have suggested that LLSVPs represent passive "piles" of thermochemically distinct material that are "swept" together by flow in the lowermost mantle driven by slabs impinging on the CMB (Garnero et al., 2016; McNamara & Zhong, 2005; Steinberger & Torsvik, 2012). Flow toward the edges of LLSVPs has been inferred in a few other regions from seismic anisotropy observations, most notably along the eastern edge of the African LLSVP (Ford et al., 2015; Reiss et al., 2019). Some studies have argued that flow at the base of the mantle directed toward the Perm Anomaly is a possibility as well based on seismic observations (Hu & He, 2019; Long & Lynner, 2015) that sampled just to the south of our study region.

We can also look to the predictions made about flow at the base of the mantle in our study region by global mantle convection models. Studies that have explicitly discussed flow patterns in the lowermost mantle include work by Forte et al. (2015), who modeled instantaneous flow based on mantle density distributions inferred from seismic tomography and gravity data, and Flament (2019), who modeled global mantle flow based on input from plate reconstructions. The TX2008 model of Simmons et al. (2009) at a depth of 2,685 km predicts lowermost mantle flow beneath Siberia directed to the west with a slight upward vertical flow component, similar to inferences that have been made based on the inferred transport of MO and Km slab remnants (van der Meer et al., 2018). The Flament (2019) model, on the other hand, predicts nearly horizontal flow (with a slight upward component) directed to the south-southwest (1.2 cm/yr, oriented ~200° from north) beneath our study region, directed toward the Perm Anomaly.

Interestingly, both westward-directed flow (suggested by the Forte et al. (2015) model and by studies that have argued for westward transport of MO slab remnants; Fritzell et al., 2016; Shepard et al., 2014; van der

Meer, 2018) and south-southwestward directed flow (suggested by the Flament [2019] model and by the general notion that flow may be directed toward the Perm Anomaly) have been noted as plausible flow directions from previous seismic studies beneath Siberia. Recent work (Li, 2020) has also argued that small-scale convection near the core-mantle boundary can form hot thermal ridges when driven by subducting slabs–driving flow toward hot anomalies such as (presumably) the Perm anomaly. Li et al. (2020) suggested that such thermal ridges may enhance seismic anisotropy.

Thomas et al. (2011) suggested flow to the west (or, equivalently, to the east) as possible explanations for reflection polarity observations, while Wookey and Kendall (2008) suggested that flow directed to the south (or, equivalently, to the north) was consistent with ScS splitting observations. Tao et al. (2020) recently suggested the presence of flow directed toward the west, toward the Perm Anomaly, just to the south of our study region (∼50°N). Our modeling exercise, which has combined several different data types used in previous studies, has identified three successful models, all of which are consistent with a shear direction oriented to the south-southwest (or to the north-northeast, although that has not been suggested as a plausible flow direction based on geodynamic considerations). While each of these three models is consistent with our measurements, the dominant slip system invoked by Model A has been previously suggested as the most likely scenario for D″ seismic anisotropy (e.g., Creasy et al., 2017; Ford et al., 2015; Pisconti et al., 2019; Walker et al., 2011). The deformation geometry and flow direction suggested by Model A, which we consider to be the most likely scenario given previous constraints on post-perovskite deformation, is shown in Figure 8. We find that flow directed to the south-southwest toward the Perm Anomaly is most consistent with the suite of seismic anisotropy observations modeled in our study. The details of the possible relationships between this inferred flow regime and the slab remnants cataloged by van der Meer (2018) and others remain unclear, particularly since the MO slab remnant and a region of particularly fast isotropic velocities lie to the east of our study area (not to the north-northeast as might be expected for a slab remnant driving flow to the south-southwest). These possible relationships must be examined in future work. While Model A represents our preferred scenario, Model E (bridgmanite), also fits our observations, and while we view this case as less likely, we cannot discount it as a possibility. Recent work has shown conflicting viewpoints on whether, and under what conditions bridgmanite deformation forms CPO (e.g., Boioli et al., 2017; Miyagi & Wenk, 2016; Reali et al., 2019), and this represents an important avenue for future work.

Our inference of likely flow directed to the south-southwest, toward the Perm Anomaly, comes with some important caveats. We have assumed that the seismic anisotropic structure is laterally homogeneous within our study region, and we have not exhaustively examined all possible models for D″ seismic anisotropy, so there is room for future work. We have chosen to ignore the possible influence of small-scale 3D structures, for example, ultra-low/high velocity zones, as these features are likely too small for our phases of interest to be highly sensitive to, but future modeling work could consider such structures. While our modeling favors the CPO of post-perovskite or bridgmanite as the more likely scenarios, we cannot completely rule out CPO of ferropericlase as a possible mechanism, and further testing of more realistic ferropericlase CPO scenarios will be needed. Interestingly, when ferropericlase aggregates are deformed in experiments (e.g., Marquardt et al., 2009), or when ferropericlase textures are simulated using a VPSC approach, the bulk elastic properties are surprisingly similar to those of deformed post-perovskite aggregates (Creasy et al., 2020), even though the single-crystal elastic tensors are different (and have different symmetry). While we only examined single-phase endmember models, the actual lower mantle is made up of multiple phases, and future work on the behavior of polyphase aggregates will be necessary to understand how textures develop in the real Earth.

An interesting finding from our work is that the elastic tensors based on single-crystal elasticity tensors provide better fits to the data than those derived from VPSC modeling. The VPSC tensors are calculated based on simulating strain and texture development within a numerical framework, while our single-crystal tensors have the underlying assumption that there is a 12% alignment of grains. The behavior of the VPSC tensors is quite sensitive to the top layer of isotropic material, especially when comparing Model G versus Model H and Model I versus Model J (Figure S5–S8 in Supporting Information S1); these pairs of models only differ by the properties of the top isotropic layer. For Models G and H, the reflection measurements do not fit Model H, but provide possible orientations for Model G (Figures S5 and S6 in Supporting Information S1). Therefore, a fuller exploration of how different parameters in the VPSC modeling (e.g., strain rates,

10.1029/2021GC009924

grain alignments, relative strength of different slip systems, etc.) affect the details of the resulting elastic tensor and the corresponding reflection polarizations is worthy of future investigation.

Additionally, all our modeling is based on a ray theoretical approximation, with the simplifying assumption that the ScS phase propagation direction is perfectly horizontal at the base of the mantle. Future modeling work that explicitly includes the ScS reflection at the CMB, and explicitly takes into account the down-going and upgoing legs of the ScS phase, is needed, as is work that goes beyond ray theory and considers the full physics of wave propagation in global waveform modeling scenarios. Comparisons between full-wave simulations and ray theoretical approximations show that in many cases, ray theory is an adequate (and computationally inexpensive) strategy for modeling shear wave splitting due to lowermost mantle seismic anisotropy (e.g., Tesoniero et al., 2020). Departures from ray theory have been documented, however (e.g., Nowacki & Wookey, 2016; Tesoniero et al., 2020; Wolf et al., 2021), and a move to modeling strategies that consider full-wave propagation is desirable, despite the computational cost.

Another potential complication that deserves future attention relates to the splitting of PKS due to D″ seismic anisotropy; this phase is more complicated than SKS, due to a triplication and potential interference with SKP. More sophisticated modeling of PKS splitting, using tools that include global wavefield simulations, should allow for more nuanced interpretation of this phase in the future. Given the significant potential of PKS splitting observations to expand data coverage in studies of D″ seismic anisotropy, it is well worth investigating outside of a ray theoretical framework.

We emphasize, finally, that there are a few aspects of the splitting datasets that underpin our modeling that may warrant additional investigation in the future. As is typical of most shear wave splitting datasets, our observations contain considerable scatter (Figures 3 and 4), most likely due to the combination of noise and scattering or other wavefield complexities due to 3D structure in the context of finite-frequency effects. These effects could be more thoroughly investigated in the future, particularly in the context of full-wave modeling. Another aspect that was not considered here is the possibility of frequency dependent shear wave splitting, which has been shown to be relevant for several SKS splitting datasets (e.g., Eakin & Long, 2013; Walpole et al., 2014). The consideration of frequency dependence is potentially important particularly for the upper mantle corrections because shear wave splitting due to the upper mantle seismic anisotropy may depend on frequency. Therefore, it is important for upper mantle corrections to be calculated using the same filter parameters as being used in the measurement of the deep mantle splitting component. The consideration of frequency-dependent shear wave splitting, particularly in the context of upper mantle and using waveform modeling tools, is worthy of future exploration.

6. Summary

We analyzed a combination of previously published and new measurements of seismic anisotropy in the D″ layer beneath Siberia in order to understand the pattern of flow at the base of the mantle. We applied a novel forward modeling approach that combines diverse data types (PdP and SdS reflection polarities and shear wave splitting of ScS and PKS phases) to obtain tighter constraints on the geometry of seismic anisotropy than would be available with a single type of observation. We found that models that invoke the CPO of post-perovskite or bridgmanite were able to fit the set of observations, although all the successful models used elastic tensors based on constraints on single-crystal elasticity at relevant temperatures and pressures, rather than those based on explicit modeling of texture development. All three successful models suggest a shear direction oriented either south-southwest or north-northeast; for post-perovskite with a [100](010) dominant slip system (perhaps the most likely scenario), the shear plane is close to horizontal, dipping slightly (dip angle of $23° \pm 5°$) to the east. Based on our favored scenario (Figure 7), we suggest the presence of lowermost mantle flow directed toward the south-southwest, toward the Perm Anomaly. While the exact relationships between slab remnants in the lower mantle and the Perm Anomaly remain to be elucidated in detail, the combined seismic anisotropy dataset used in this study, and the inferences on flow gleaned from our modeling approach, should be a useful constraint for future geodynamical investigations.

Data Availability Statement

Waveform data used in this study came from the Global Seismographic Network (GSN; network code II) and were downloaded from the archive of the Data Management Center (DMC) of the Incorporated Research Institutions for Seismology (IRIS) (https://doi.org/10.7914/SN/II). IRIS Data Services are funded through the Seismological Facilities for the Advancement of Geoscience and EarthScope (SAGE) Proposal of the National Science Foundation (NSF) under Cooperative Agreement EAR-1261681. Supporting Information S1 is also appended in a Mendeley data repository (http://dx.doi.org/10.17632/63jxdbv9t2.1).

Acknowledgments
The authors acknowledge funding from NSF via a Graduate Research Fellowship to N. Creasy DGE-1122492 and via grant EAR-1547499 to M. D. Long, and from the European Union's Horizon 2020 research and innovation program under the Marie Slodowska-Curie grant agreement No. 642029-ITN CREEP (A. Pisconti). We thank two anonymous reviewers for their constructive comments and contributions.

References

Amodeo, J., Carrez, P., & Cordier, P. (2012). Modelling the effect of pressure on the critical shear stress of MgO single crystals. *Philosophical Magazine*, *92*(12), 1523–1541. https://doi.org/10.1080/14786435.2011.652689

Asplet, J., Wookey, J., & Kendall, M. (2020). A potential post-perovskite province in D″ beneath the Eastern Pacific: Evidence from new analysis of discrepant SKS–SKKS shear-wave splitting. *Geophysical Journal International*, *221*(3), 2075–2090. https://doi.org/10.1093/gji/ggaa114

Boioli, F., Carrez, P., Cordier, P., Devincre, B., Gouriet, K., Hirel, P., et al. (2017). Pure climb creep mechanism drives flow in Earth's lower mantle. *Science Advances*, *3*(3), e1601958. https://doi.org/10.1126/sciadv.1601958

Bower, D. J., Gurnis, M., & Seton, M. (2013). Lower mantle structure from paleogeographically constrained dynamic Earth models. *Geochemistry, Geophysics, Geosystems*, *14*(1), 44–63. https://doi.org/10.1029/2012GC004267

Bowman, J. R., & Ando, M. (1987). Shear-wave splitting in the upper-mantle wedge above the Tonga subduction zone. *Geophysical Journal International*, *88*(1), 25–41. https://doi.org/10.1111/j.1365-246X.1987.tb01367.x

Browaeys, J. T., & Chevrot, S. (2004). Decomposition of the elastic tensor and geophysical applications. *Geophysical Journal International*, *159*(2), 667–678. https://doi.org/10.1111/j.1365-246X.2004.02415.x

Chevrot, S. (2000). Multichannel analysis of shear wave splitting. *Journal of Geophysical Research: Solid Earth*, *105*(B9), 21579–21590. https://doi.org/10.1029/2000JB900199

Cordier, P., Amodeo, J., & Carrez, P. (2012). Modelling the rheology of MgO under Earth's mantle pressure, temperature and strain rates. *Nature*, *481*(7380), 177–180. https://doi.org/10.1038/nature10687

Cottaar, S., & Lekic, V. (2016). Morphology of seismically slow lower-mantle structures. *Geophysical Journal International*, *207*(2), 1122–1136. https://doi.org/10.1093/gji/ggw324

Couper, S., Speziale, S., Marquardt, H., Liermann, H.-P., & Miyagi, L. (2020). Does heterogeneous strain act as a control on seismic anisotropy in Earth's lower mantle? *Frontiers of Earth Science*, *8*. https://doi.org/10.3389/feart.2020.540449

Creasy, N., Long, M. D., & Ford, H. A. (2017). Deformation in the lowermost mantle beneath Australia from observations and models of seismic anisotropy. *Journal of Geophysical Research: Solid Earth*, *122*(7), 5243–5267. https://doi.org/10.1002/2016JB013901

Creasy, N., Miyagi, L., & Long, M. D. (2020). A library of elastic tensors for lowermost mantle seismic anisotropy studies and comparison with seismic observations. *Geochemistry, Geophysics, Geosystems*, *21*(4), e2019GC008883. https://doi.org/10.1029/2019GC008883

Creasy, N., Pisconti, A., Long, M. D., Thomas, C., & Wookey, J. (2019). Constraining lowermost mantle anisotropy with body waves: A synthetic modelling study. *Geophysical Journal International*, *217*(2), 766–783. https://doi.org/10.1093/gji/ggz049

Crotwell, H. P., Owens, T. J., & Ritsema, J. (1999). The TauP Toolkit: Flexible seismic travel-time and ray-path utilities. *Seismological Research Letters*, *70*(2), 154–160. https://doi.org/10.1785/gssrl.70.2.154

Deng, J., Long, M. D., Creasy, N., Wagner, L., Beck, S., Zandt, G., et al. (2017). Lowermost mantle anisotropy near the eastern edge of the Pacific LLSVP: Constraints from SKS–SKKS splitting intensity measurements. *Geophysical Journal International*, *210*(2), 774–786. https://doi.org/10.1093/gji/ggx190

Dziewonski, A. M., & Anderson, D. L. (1981). Preliminary reference Earth model. *Physics of the Earth and Planetary Interiors*, *25*(4), 297–356. https://doi.org/10.1016/0031-9201(81)90046-7

Eakin, C. M., & Long, M. D. (2013). Complex anisotropy beneath the Peruvian flat slab from frequency-dependent, multiple-phase shear wave splitting analysis: Complex anisotropy beneath Peru. *Journal of Geophysical Research: Solid Earth*, *118*(9), 4794–4813. https://doi.org/10.1002/jgrb.50349

Flament, N. (2019). Present-day dynamic topography and lower-mantle structure from palaeogeographically constrained mantle flow models. *Geophysical Journal International*, *216*(3), 2158–2182. https://doi.org/10.1093/gji/ggy526

Flament, N., Williams, S., Müller, R. D., Gurnis, M., & Bower, D. J. (2017). Origin and evolution of the deep thermochemical structure beneath Eurasia. *Nature Communications*, *8*(1), 14164. https://doi.org/10.1038/ncomms14164

Ford, H. A., Long, M. D., He, X., & Lynner, C. (2015). Lowermost mantle flow at the eastern edge of the African large low shear velocity province. *Earth and Planetary Science Letters*, *420*, 12–22. https://doi.org/10.1016/j.epsl.2015.03.029

Forte, A., Simmons, N., & Grand, S. (2015). Constraints on 3-D seismic models from global geodynamic observables: Implications for the global mantle convective flow. *Treatise on Geophysics, Seismology and the Structure of the Earth*, *1*, 853–907. https://doi.org/10.1016/B978-0-444-53802-4.00028-2

Fritzell, E. H., Bull, A. L., & Shephard, G. E. (2016). Closure of the Mongol–Okhotsk Ocean: Insights from seismic tomography and numerical modelling. *Earth and Planetary Science Letters*, *445*, 1–12. https://doi.org/10.1016/j.epsl.2016.03.042

Garnero, E. J., & Lay, T. (1997). Lateral variations in lowermost mantle shear wave anisotropy beneath the north Pacific and Alaska. *Journal of Geophysical Research: Solid Earth*, *102*(B4), 8121–8135. https://doi.org/10.1029/96JB03830

Garnero, E. J., McNamara, A. K., & Shim, S.-H. (2016). Continent-sized anomalous zones with low seismic velocity at the base of Earth's mantle. *Nature Geoscience*, *9*(7), 481–489. https://doi.org/10.1038/ngeo2733

Girard, J., Chen, J., & Raterron, P. (2012). Deformation of periclase single crystals at high pressure and temperature: Quantification of the effect of pressure on slip-system activities. *Journal of Applied Physics*, *111*(11), 112607. https://doi.org/10.1063/1.4726200

Golonka, J., Bocharova, N. Y., Ford, D., Edrich, M. E., Bednarczyk, J., & Wildharber, J. (2003). Paleogeographic reconstructions and basins development of the Arctic. *Marine and Petroleum Geology*, *20*(3), 211–248. https://doi.org/10.1016/S0264-8172(03)00043-6

Grund, M. (2017). StackSplit-a plugin for multi-event shear wave splitting analyses in SplitLab. *Computers & Geosciences*, *105*, 43–50. https://doi.org/10.1016/j.cageo.2017.04.015

Grund, M., & Ritter, J. R. (2020). Shear-wave splitting beneath Fennoscandia—Evidence for dipping structures and laterally varying multilayer anisotropy. *Geophysical Journal International*, *223*(3), 1525–1547. https://doi.org/10.1093/gji/ggaa388

Grund, M., & Ritter, J. R. R. (2019). Widespread seismic anisotropy in Earth's lowermost mantle beneath the Atlantic and Siberia. *Geology*, *47*(2), 123–126. https://doi.org/10.1130/G45514.1

Guest, W. S., & Kendall, J. M. (1993). Modeling seismic waveforms in anisotropic media using Maslov asymptotic theory. *Journal of Exploratory Geophysics*, *29*, 78–92.

Hassan, R., Flament, N., Gurnis, M., Bower, D. J., & Müller, D. (2015). Provenance of plumes in global convection models. *Geochemistry, Geophysics, Geosystems*, *16*(5), 1465–1489. https://doi.org/10.1002/2015GC005751

He, X., & Long, M. D. (2011). Lowermost mantle anisotropy beneath the northwestern Pacific: Evidence from PcS, ScS, SKS, and SKKS phases. *Geochemistry, Geophysics, Geosystems*, *12*(12), a–n. https://doi.org/10.1029/2011GC003779

Hirose, K., Nagaya, Y., Merkel, S., & Ohishi, Y. (2010). Deformation of $MnGeO_3$ post-perovskite at lower mantle pressure and temperature. *Geophysical Research Letters*, *37*(20). https://doi.org/10.1029/2010GL044977

Hu, J., & He, X. (2019). Seismic evidence for a paleoslab in the D' layer residing adjacent to the southeastern edge of the perm anomaly. *Geochemistry, Geophysics, Geosystems*, *20*(4), 2040–2052. https://doi.org/10.1029/2019GC008195

Immoor, J., Marquardt, H., Miyagi, L., Lin, F., Speziale, S., Merkel, S., et al. (2018). Evidence for {100}<011> slip in ferropericlase in Earth's lower mantle from high-pressure/high-temperature experiments. *Earth and Planetary Science Letters*, *489*, 251–257. https://doi.org/10.1016/j.epsl.2018.02.045

Karki, B. B., Wentzcovitch, R. M., de Gironcoli, S., & Baroni, S. (1999). First-principles determination of elastic anisotropy and wave velocities of MgO at lower mantle conditions. *Science*, *286*(5445), 1705–1707. https://doi.org/10.1126/science.286.5445.1705

Kendall, J.-M., & Silver, P. G. (1996). Constraints from seismic anisotropy on the nature of the lowermost mantle. *Nature*, *381*(6581), 409–412. https://doi.org/10.1038/381409a0

Kubo, A., Kiefer, B., Shim, S.-H., Shen, G., Prakapenka, V. B., & Duffy, T. S. (2008). Rietveld structure refinement of $MgGeO_3$ post-perovskite phase to 1 Mbar. *American Mineralogist*, *93*(7), 965–976. https://doi.org/10.2138/am.2008.2691

Lebensohn, R. A., & Tomé, C. N. (1994). A self-consistent viscoplastic model: Prediction of rolling textures of anisotropic polycrystals. *Materials Science and Engineering: A*, *175*(1), 71–82. https://doi.org/10.1016/0921-5093(94)91047-2

Lekic, V., Cottaar, S., Dziewonski, A., & Romanowicz, B. (2012). Cluster analysis of global lower mantle tomography: A new class of structure and implications for chemical heterogeneity. *Earth and Planetary Science Letters*, *357*(358), 68–77. https://doi.org/10.1016/j.epsl.2012.09.014

Li, M. (2020). The formation of hot thermal anomalies in cold subduction-influenced regions of Earth's lowermost mantle. *Journal of Geophysical Research: Solid Earth*, *125*(6), e2019JB019312. https://doi.org/10.1029/2019JB019312

Liu, K. H., & Gao, S. S. (2013). Making reliable shear-wave splitting measurements. *Bulletin of the Seismological Society of America*, *103*(5), 2680–2693. https://doi.org/10.1785/0120120355

Long, M. D. (2009). Complex anisotropy in D″ beneath the eastern Pacific from SKS–SKKS splitting discrepancies. *Earth and Planetary Science Letters*, *283*(1–4), 181–189. https://doi.org/10.1016/j.epsl.2009.04.019

Long, M. D., & Becker, T. W. (2010). Mantle dynamics and seismic anisotropy. *Earth and Planetary Science Letters*, *297*(3–4), 341–354. https://doi.org/10.1016/j.epsl.2010.06.036

Long, M. D., & Lynner, C. (2015). Seismic anisotropy in the lowermost mantle near the perm anomaly. *Geophysical Research Letters*, *42*(17), 7073–7080. https://doi.org/10.1002/2015GL065506

Lutz, K. A., Long, M. D., Creasy, N., & Deng, J. (2020). Seismic anisotropy in the lowermost mantle beneath North America from SKS-SKKS splitting intensity discrepancies. *Physics of the Earth and Planetary Interiors*, *305*, 106504. https://doi.org/10.1016/j.pepi.2020.106504

Lynner, C., & Long, M. D. (2013). Sub-slab seismic anisotropy and mantle flow beneath the Caribbean and Scotia subduction zones: Effects of slab morphology and kinematics. *Earth and Planetary Science Letters*, *361*, 367–378. https://doi.org/10.1016/j.epsl.2012.11.007

Lynner, C., & Long, M. D. (2014). Lowermost mantle anisotropy and deformation along the boundary of the African LLSVP. *Geophysical Research Letters*, *41*(10), 3447–3454. https://doi.org/10.1002/2014gl059875

Marquardt, H., Speziale, S., Reichmann, H. J., Frost, D. J., & Schilling, F. R. (2009). Single-crystal elasticity of $(Mg_{0.9}Fe_{0.1})$ O to 81 GPa. *Earth and Planetary Science Letters*, *287*(3-4), 345–352. https://doi.org/10.1016/j.epsl.2009.08.017

McNamara, A. K., & Zhong, S. (2005). Thermochemical structures beneath Africa and the Pacific Ocean. *Nature*, *437*(7062), 1136–1139. https://doi.org/10.1038/nature04066

Meade, C., Silver, P. G., & Kaneshima, S. (1995). Laboratory and seismological observations of lower mantle isotropy. *Geophysical Research Letters*, *22*(10), 1293–1296. https://doi.org/10.1029/95GL01091

Miyagi, L., Kanitpanyacharoen, W., Kaercher, P., Lee, K. K. M., & Wenk, H.-R. (2010). Slip Systems in $MgSiO_3$ post-perovskite: implications for D′′ anisotropy. *Science*, *329*(5999), 1639–1641. https://doi.org/10.1126/science.1192465

Miyagi, L., Nishiyama, N., Wang, Y., Kubo, A., West, D. V., Cava, R. J., et al. (2008). Deformation and texture development in $CaIrO_3$ post-perovskite phase up to 6 GPa and 1300 K. *Earth and Planetary Science Letters*, *268*(3), 515–525. https://doi.org/10.1016/j.epsl.2008.02.005

Miyagi, L., & Wenk, H.-R. (2016). Texture development and slip systems in bridgmanite and bridgmanite + ferropericlase aggregates. *Physics and Chemistry of Minerals*, *43*(8), 597–613. https://doi.org/10.1007/s00269-016-0820-y

Nataf, H.-C., & Houard, S. (1993). Seismic discontinuity at the top of D″: A world-wide feature? *Geophysical Research Letters*, *20*(21), 2371–2374. https://doi.org/10.1029/93GL02686

Niu, F., & Perez, A. M. (2004). Seismic anisotropy in the lower mantle: A comparison of waveform splitting of SKS and SKKS. *Geophysical Research Letters*, *31*(24). https://doi.org/10.1029/2004GL021196

Nowacki, A. (2013). Predicting lowermost mantle anisotropy using models of mantle flow. In *Plate deformation from cradle to grave* (pp. 123–149). Springer Berlin Heidelberg. https://doi.org/10.1007/978-3-642-34842-6_5

Nowacki, A., & Wookey, J. (2016). The limits of ray theory when measuring shear wave splitting in the lowermost mantle with ScS waves. *Geophysical Journal International*, *207*(3), 1573–1583. https://doi.org/10.1093/gji/ggw358

Nowacki, A., Wookey, J., & Kendall, J.-M. (2010). Deformation of the lowermost mantle from seismic anisotropy. *Nature*, *467*(7319), 1091–1094. https://doi.org/10.1038/nature09507

Nowacki, A., Wookey, J., & Kendall, J.-M. (2011). New advances in using seismic anisotropy, mineral physics and geodynamics to understand deformation in the lowermost mantle. *Journal of Geodynamics*, *52*(3–4), 205–228. https://doi.org/10.1016/j.jog.2011.04.003

Pisconti, A., Thomas, C., & Wookey, J. (2019). Discriminating between causes of D″ anisotropy using reflections and splitting measurements for a single path. *Journal of Geophysical Research: Solid Earth*, *124*(5), 4811–4830. https://doi.org/10.1029/2018JB016993

Rao, P. R., & Kumar, R. (2014). Seismic evidence for slab graveyards atop the core mantle boundary beneath the Indian Ocean geoid low. *Physics of the Earth and Planetary Interiors*, *236*, 52–59. https://doi.org/10.1016/j.pepi.2014.08.005

Reali, R., Van Orman, J. A., Pigott, J. S., Jackson, J. M., Boioli, F., Carrez, P., & Cordier, P. (2019). The role of diffusion-driven pure climb creep on the rheology of bridgmanite under lower mantle conditions. *Scientific Reports*, *9*(1), 2053. https://doi.org/10.1038/s41598-018-38449-8

Reiss, M. C., Long, M. D., & Creasy, N. (2019). Lowermost mantle anisotropy beneath africa from differential SKS-SKKS shear-wave splitting. *Journal of Geophysical Research: Solid Earth*, *124*(8), 8540–8564. https://doi.org/10.1029/2018JB017160

Romanowicz, B., & Wenk, H.-R. (2017). Anisotropy in the deep Earth. *Physics of the Earth and Planetary Interiors*, *269*, 58–90. https://doi.org/10.1016/j.pepi.2017.05.005

Ross, A. R., Thybo, H., & Solidilov, L. N. (2004). Reflection seismic profiles of the core-mantle boundary. *Journal of Geophysical Research: Solid Earth*, *109*(B8). https://doi.org/10.1029/2003jb002515

Rost, S., & Thomas, C. (2002). Array seismology: Methods and applications. *Reviews of Geophysics*, *40*(3), 2-1–2-27. https://doi.org/10.1029/2000RG000100

Scherbaum, F., Krüger, F., & Weber, M. (1997). Double beam imaging: Mapping lower mantle heterogeneities using combinations of source and receiver arrays. *Journal of Geophysical Research: Solid Earth*, *102*(B1), 507–522. https://doi.org/10.1029/96JB03115

Shephard, G. E., Flament, N., Williams, S., Seton, M., Gurnis, M., & Müller, R. D. (2014). Circum-Arctic mantle structure and long-wavelength topography since the Jurassic. *Journal of Geophysical Research: Solid Earth*, *119*(10), 7889–7908. https://doi.org/10.1002/2014JB011078

Silver, P. G., & Chan, W. W. (1991). Shear wave splitting and subcontinental mantle deformation. *Journal of Geophysical Research: Solid Earth*, *96*(B10), 16429–16454. https://doi.org/10.1029/91JB00899

Silver, P. G., & Savage, M. K. (1994). The interpretation of shear-wave splitting parameters in the presence of two anisotropic layers. *Geophysical Journal International*, *119*(3), 949–963. https://doi.org/10.1111/j.1365-246X.1994.tb04027.x

Simmons, N. A., Forte, A. M., & Grand, S. P. (2009). Joint seismic, geodynamic and mineral physical constraints on three-dimensional mantle heterogeneity: Implications for the relative importance of thermal versus compositional heterogeneity. *Geophysical Journal International*, *177*(3), 1284–1304. https://doi.org/10.1111/j.1365-246X.2009.04133.x

Skemer, P., & Hansen, L. N. (2016). Inferring upper-mantle flow from seismic anisotropy: An experimental perspective. *Tectonophysics*, *668–669*, 1–14. https://doi.org/10.1016/j.tecto.2015.12.003

Stackhouse, S., Brodholt, J. P., Wookey, J., Kendall, J.-M., & Price, G. D. (2005). The effect of temperature on the seismic anisotropy of the perovskite and post-perovskite polymorphs of $MgSiO_3$. *Earth and Planetary Science Letters*, *230*(1–2), 1–10. https://doi.org/10.1016/j.epsl.2004.11.021

Stampfli, G. M., & Borel, G. D. (2004). The TRANSMED transects in space and time: Constraints on the paleotectonic evolution of the Mediterranean domain. In W. Cavazza, F. Roure, W. Spakman, G. M. Stampfli, & P. A. Ziegler (Eds.), *The TRANSMED Atlas. The Mediterranean region from crust to mantle: Geological and geophysical framework of the Mediterranean and the surrounding areas* (pp. 53–80). Springer. https://doi.org/10.1007/978-3-642-18919-7_3

Steinberger, B., & Torsvik, T. H. (2012). A geodynamic model of plumes from the margins of large low shear velocity provinces. *Geochemistry, Geophysics, Geosystems*, *13*(1). https://doi.org/10.1029/2011GC003808

Tao, J., Hu, J., Jin, C., & He, X. (2020). Seismic evidence links the subducted Mongol-Okhotsk slab to deformation in D″ near the northeastern margin of the perm anomaly. *Tectonophysics*, *774*, 228297. https://doi.org/10.1016/j.tecto.2019.228297

Tesoniero, A., Leng, K., Long, D. M., & Nissen-Meyer, T. (2020). Full wave sensitivity of SK (K) S phases to arbitrary anisotropy in the upper and lower mantle. *Geophysical Journal International*, *222*(1), 412–435. https://doi.org/10.1093/gji/ggaa171

Thomas, C., & Kendall, J. M. (2002). The lowermost mantle beneath northern Asia—II. Evidence for lower-mantle anisotropy. *Geophysical Journal International*, *151*(1), 296–308. https://doi.org/10.1046/j.1365-246X.2002.01760.x

Thomas, C., & Weber, M. (1997). P velocity heterogeneities in the lower mantle determined with the German Regional Seismic Network: Improvement of previous models and results of 2D modelling. *Physics of the Earth and Planetary Interiors*, *101*(1), 105–117. https://doi.org/10.1016/S0031-9201(96)03245-1

Thomas, C., Wookey, J., Brodholt, J., & Fieseler, T. (2011). Anisotropy as cause for polarity reversals of D″ reflections. *Earth and Planetary Science Letters*, *307*(3), 369–376. https://doi.org/10.1016/j.epsl.2011.05.011

Tomurtogoo, O., Windley, B. F., Kröner, A., Badarch, G., & Liu, D. Y. (2005). Zircon age and occurrence of the Adaatsag ophiolite and Muron shear zone, central Mongolia: Constraints on the evolution of the Mongol–Okhotsk ocean, suture and orogen. *Journal of the Geological Society*, *162*(1), 125–134. https://doi.org/10.1144/0016-764903-146

Tsujino, N., Nishihara, Y., Yamazaki, D., Seto, Y., Higo, Y., & Takahashi, E. (2016). Mantle dynamics inferred from the crystallographic preferred orientation of bridgmanite. *Nature*, *539*(7627), 81–84. https://doi.org/10.1038/nature19777

van der Meer, D. G., Spakman, W., van Hinsbergen, D. J. J., Amaru, M. L., & Torsvik, T. H. (2010). Towards absolute plate motions constrained by lower-mantle slab remnants. *Nature Geoscience*, *3*(1), 36–40. https://doi.org/10.1038/ngeo708

van der Meer, D. G., van Hinsbergen, D. J. J., & Spakman, W. (2018). Atlas of the underworld: Slab remnants in the mantle, their sinking history, and a new outlook on lower mantle viscosity. *Tectonophysics*, *723*, 309–448. https://doi.org/10.1016/j.tecto.2017.10.004

Van der Voo, R., Spakman, W., & Bijwaard, H. (1999). Mesozoic subducted slabs under Siberia. *Nature*, *397*(6716), 246–249. https://doi.org/10.1038/16686

Walker, A. M., Forte, A. M., Wookey, J., Nowacki, A., & Kendall, J.-M. (2011). Elastic anisotropy of D″ predicted from global models of mantle flow. *Geochemistry, Geophysics, Geosystems*, *12*(10). https://doi.org/10.1029/2011GC003732

Walker, A. M., & Wookey, J. (2012). MSAT—A new toolkit for the analysis of elastic and seismic anisotropy. *Computers & Geosciences*, *49*, 81–90. https://doi.org/10.1016/j.cageo.2012.05.031

Walpole, J., Wookey, J., Masters, G., & Kendall, J. M. (2014). A uniformly processed data set of SKS shear wave splitting measurements: A global investigation of upper mantle anisotropy beneath seismic stations. *Geochemistry, Geophysics, Geosystems*, *15*(5), 1991–2010. https://doi.org/10.1002/2014gc005278

Walsh, E., Arnold, R., & Savage, M. K. (2013). Silver and Chan revisited. *Journal of Geophysical Research: Solid Earth*, *118*(10), 5500–5515. https://doi.org/10.1002/jgrb.50386

Weber, M. (1993). P- and S-wave reflections from anomalies in the lowermost mantle. *Geophysical Journal International*, *115*(1), 183–210. https://doi.org/10.1111/j.1365-246X.1993.tb05598.x

Weber, M., & Davis, J. P. (1990). Evidence of a laterally variable lower mantle structure from P- and S-waves. *Geophysical Journal International*, *102*(1), 231–255. https://doi.org/10.1111/j.1365-246X.1990.tb00544.x

Wentzcovitch, R. M., Tsuchiya, T., & Tsuchiya, J. (2006). $MgSiO_3$ postperovskite at D″ conditions. *Proceedings of the National Academy of Sciences of the United States of America*, *103*(3), 543–546. https://doi.org/10.1073/pnas.0506879103

Wolf, A. S., Jackson, J. M., Dera, P., & Prakapenka, V. B. (2015). The thermal equation of state of (Mg, Fe)SiO_3 bridgmanite (perovskite) and implications for lower mantle structures. *Journal of Geophysical Research: Solid Earth*, *120*(11), 7460–7489. https://doi.org/10.1002/2015JB012108

Wolf, J., Long, M. D., Leng, K., & Nissen-Meyer, T. (2021). Sensitivity of SK (K) S and ScS phases to heterogeneous anisotropy in the lowermost mantle from global wavefield simulations. *Geophysical Journal International*, *228*(1), 366–386. https://doi.org/10.1093/gji/ggab347

Wookey, J., & Kendall, J. M. (2008). Constraints on lowermost mantle mineralogy and fabric beneath Siberia from seismic anisotropy. *Earth and Planetary Science Letters*, *275*(1–2), 32–42. https://doi.org/10.1016/j.epsl.2008.07.049

Wookey, J., Kendall, J.-M., & Rümpker, G. (2005). Lowermost mantle anisotropy beneath the north Pacific from differential S—ScS splitting. *Geophysical Journal International*, *161*(3), 829–838. https://doi.org/10.1111/j.1365-246X.2005.02623.x

Wüstefeld, A., & Bokelmann, G. (2007). Null detection in shear-wave splitting measurements. *Bulletin of the Seismological Society of America*, *97*(4), 1204–1211. https://doi.org/10.1111/j.1365-246X.2005.02623.x

Wüstefeld, A., Bokelmann, G., Zaroli, C., & Barruol, G. (2008). SplitLab: A shear-wave splitting environment in Matlab. *Computers & Geosciences*, *34*(5), 515–528. https://doi.org/10.1016/j.cageo.2007.08.002

Yamazaki, D., Yoshino, T., Ohfuji, H., Ando, J., & Yoneda, A. (2006). Origin of seismic anisotropy in the D″ layer inferred from shear deformation experiments on post-perovskite phase. *Earth and Planetary Science Letters*, *252*(3), 372–378. https://doi.org/10.1016/j.epsl.2006.10.004